Progress in Nuclear Energy 154 (2022) 104460

Contents lists available at ScienceDirect

Progress in Nuclear Energy

journal homepage: www.elsevier.com/locate/pnucene

Wetting-induced volumetric collapse of UO_2 powder beds and the consequence on transient nuclear criticality excursions

G.S. Jones *, C.M. Cooling, M.M.R. Williams, M.D. Eaton

Imperial College London, Nuclear Engineering Group, Department of Mechanical Engineering, City and Guilds Building, Exhibition Road, London, SW7 2BX, United Kingdom

ARTICLE INFO

Dataset link: https://doi.org/10.5281/zenodo.7104999

Keywords:
Nuclear criticality safety analysis and assessment
Fissile powder bed
Volumetric collapse
Slumping
Transient nuclear criticality excursion
Point neutron kinetics
Phenomenologically thermal hydraulics

ABSTRACT

Mathematical and computational models are proposed to simulate wetting-induced volumetric collapse of fissile powder beds. Slumping, nuclear thermal hydraulics, radiolytic gas, and steam production models are coupled with point neutron kinetics to investigate transient nuclear criticality excursions in two 5-wt% enriched UO_2 fissile powder beds with varying levels of wetting-induced volumetric collapse. The two beds are distinguished by their mean powder particle size of 30 μm and 100 μm. For the UO_2 powder beds modelled, the re-distribution of UO_2 powder and moderator due to slumping introduced a negative reactivity into the system. This increased the amount of time taken for a delayed critical state to be reached once infiltration began, and also reduced the total fission energy generated over the course of the simulated transient. The total fission energy generated ranged from 42 MJ to 48 MJ 100 seconds after the initial nuclear criticality excursion was observed for the 30 μm sized UO_2 powder bed. The fission energy of the larger sized powder bed (100 μm), varied from 42 MJ to 57 MJ. Larger discrepancies between the slumped and un-slumped initial peak power are predicted. Peak powers varied from 29.2 MW to 106 MW for the smaller-sized powder particles, whereas for larger particles, the peak powers varied from 255 MW to 501 MW.

1. Introduction

In nuclear fuel fabrication facilities, various fissile powders, including but not limited to uranium dioxide (UO_2), Yellowcake (predominantly, tri-uranium octoxide or U_3O_8) and Mixed OXides (MOX), are commonly found with varying levels of enrichment (IAEA, 2010). The International Atomic Energy Authority (IAEA) highlight a fundamental requirement for these nuclear fuel fabrication facilities to provide preventative and mitigative measures, to minimise the risk of unexpected radiological exposure as a result of an inadvertent, self-sustaining, nuclear chain reaction involving fissile material, including powders (IAEA, 2010).

An important type of accident to acknowledge for emergency planning and preparedness of nuclear fuel fabrication facilities is that of a fire or explosion in the facility (IAEA, 2008). The scope of potential fire hazards has been noted by Datta (1991) to be wide-ranging. These include the use of combustible solvents in uranium mills, acids with unfavourable ignition characteristics under certain conditions in uranium hexa-fluoride (UF_6) facilities and the general use of products such as anhydrous ammonia and hydrogen in fuel fabrication facilities (Datta, 1991).

The IAEA emphasise the importance of providing fire-suppression systems, such as fire-sprinklers in certain areas, to mitigate the effects of an accidental fire in fuel fabrication facilities (IAEA, 2008). Furthermore, the U.S. Department of Energy (DoE) notes in Raap et al. (2014) that U.S. regulations require automatic fire-suppression systems in nuclear facilities, and commonly this is via water-based suppression. However, it is also noted by Raap et al. (2014), Doucet et al. (2003), Sakai et al. (2004) and Duhamel et al. (2004) that this introduces the potential for a wetting-induced nuclear criticality excursion due to water from the fire-suppression sprinklers, acting as moderator, impinging on the fissile powder, that is housed in cylindrical vessels within these facilities.

Double contingency measures applied to mitigate the risk of a wetting-induced reactivity insertion include applying sub-critical packaging limits and the use of moderating inserts, as well as using sealed containers to store the fissile powder (IAEA, 2008). However, in the case that these double contingency measures fail, there is a risk that a water-based fire-suppression system may lead to a nuclear criticality excursion, by increasing moderation within a fissile powder bed. Both conventional fire sprinkler systems and more modern water mist systems may lead to increased levels of moderation around

* Corresponding author.
E-mail address: g.jones18@imperial.ac.uk (G.S. Jones).

https://doi.org/10.1016/j.pnucene.2022.104460
Received 12 January 2022; Received in revised form 22 September 2022; Accepted 10 October 2022
Available online 3 November 2022

Nomenclature

Latin Symbols

$A_{i,j}$	Interfacial area between material, i, and material, j [m^2]
c	Gas advection speed empirical parameter [–]
C_i	Delayed neutron precursor concentration for group i [precursors cm^{-3}]
c_i	Specific heat capacity of material, i [J kg^{-1} K^{-1}]
D	Neutron diffusion coefficient [cm]
d_i	Spherical diameter of part of material, i [m]
$D_{t,i}$	Turbulent mixing coefficient of region, i [m^2 s^{-1}]
E_ψ	Elastic modulus due to matric potential [Pa]
e_{abs}	Absolute ODE solver error tolerance [–]
E_{fast}	Fast neutron energy [eV]
E_f	Energy generated per fission [J $fission^{-1}$]
E_i	Heat transfer rate for thermal process, i [J s^{-1}]
e_{rel}	Relative ODE solver error tolerance [–]
E_{therm}	Thermal neutron energy [eV]
f_{imm}	Powder bed immersion fraction [–]
f_{slump}	Slumping fraction [–]
$G(H_2)$	Volumetric yield of hydrogen from radiolysis [m^3 J^{-1}]
h_ψ	Matric head [m]
H_i	Region height, i [m]
$h_{l,v}$	Latent heat of vapourisation [J kg^{-1}]
$h_{p,v}$	Powder boiling heat transfer coefficient [W m^{-2} K^{-1}]
$h_{p,w}$	Powder–water convective heat transfer coefficient [W m^{-2} K^{-1}]
k	Permeability of powder bed [m^2]
$K_{b,0}$	Gas advection speed empirical parameter [–]
k_b	Boltzmann constant [eV K^{-1}]
k_{eff}	Effective multiplication factor [–]
$K_{sat,e}$	Saturated hydraulic conductivity [m s^{-1}]
m_2^s	Compressibility modulus of powder bed due to wetting [Pa^{-1}]
$M_{i,j}$	Mass of material, i, in region, j [kg]
Mo	Morton Number [–]
N	Neutron population [neutrons]
n	Neutron density [neutrons (cm^{-3} · UO_2)]
n_c	Gas advection speed empirical parameter [–]
$N_{p,i}$	Number of powder particles present in region, i [–]
P	Energy generation rate (fission power) [J s^{-1}]
R	Powder drum radius [m]
R_{fiss}	Range of fission fragments [m]
R_i	Reactivity of component, i [$]
S_A	Specific surface area [m^{-1}]
s_n	Intrinsic neutron source density [neutrons s^{-1} (cm^{-3} · UO_2)]
$S_{w,0}$	Initial dry powder region saturation [–]
t	Time [s]
T_0	Reference temperature [K]
$T_{i,j}$	Temperature of material, i, in region, j [K]
T_I	Powder–water interface temperature [K]
T_{sat}	Water boiling temperature [K]
u_a	Pore-air pressure [Pa]
U_i	Superficial velocity of material, i [m s^{-1}]
U_{slump}	Slumping superficial velocity [m s^{-1}]
$U_{w,in}$	Water impinging rate from fire sprinkler [m s^{-1}]
$U_{w,sus}$	Net water flow rate through pooled water region [m s^{-1}]
u_w	Pore-water pressure [Pa]
$v_{f,i,j}$	Volume fraction of material, i, in region, j [–]
$V_{i,j}$	Volume of gas of material, i, in region, j [m^3]
V_n	Prompt neutron speed, with energy E [cm s^{-1}]

Greek Symbols

$\bar{\nu}$	Average number of neutrons produced per prompt fission [neutrons $fission^{-1}$]
$\bar{\phi}$	Normalised scalar neutron flux distribution [cm^{-1}]
β_{eff}	Total effective delayed neutron fraction [–]
β_i	Delayed neutron fraction for precursor group, i [–]
χ_p	Prompt fission energy spectrum [–]
ΔS_w	Change in saturation across wetting front [–]
ϵ_v	Volumetric strain due to wetting [–]
η	Thermal expansion coefficient of water [K^{-1}]
κ_i	Thermal conductivity of material, i [W m^{-1} K^{-1}]
Λ	Mean generation time [s]
λ_i	Decay constant for precursor group i [s^{-1}]
μ_i	Dynamic viscosity of material, i [Pa s]
ν_p	Poisson's ratio of powder bed [–]
ψ	Matric suction [Pa]
$\rho_{i,bulk}$	Bulk density of material, i [kg m^{-3}]
$\rho_{i,th}$	Theoretical density of material, i [kg m^{-3}]
σ	Water surface tension [N m^{-1}]
Σ_a	Macroscopic neutron absorption cross-section [cm^{-1}]

the fissile powder (Holmes and McLaughlin, 1994). Monte Carlo simulations by Handley (1972), investigating water-sprinkled arrays of highly enriched uranium metal, found that there is a dependency between the mass of fissile material and the bulk density of water, from the sprinkler system, surrounding the highly enriched uranium. The possibility of this type of inadvertent transient nuclear criticality excursion requires mitigation, as noted by the American National Standard ANSI/ANS-8.1 (ANS, 2018).

Mathematical and computational models of varying computational complexity, investigating this type of transient nuclear criticality excursion, have been developed (Basoglu, 1992; Basoglu et al., 1994;

Σ_f	Macroscopic neutron fission cross-section [cm^{-1}]
Σ_s	Macroscopic neutron scattering cross-section [cm^{-1}]
Σ_t	Macroscopic neutron total cross-section [cm^{-1}]

Subscripts

0	Initial value
boil	Boiling
b	Gas bubble
convec	Inter-phase convection
dp	Dry powder region
eff	Effective region property
gen	Thermal energy generation
g	Total gas
imm	Water infiltration reactivity component
p	Fissile powder
rg	Radiolytic gas
slump	Slumping reactivity component
sus	Pooled water region
th	Thermal reactivity component
T	Total reactivity component
void	Void reactivity component
v	Water vapour
wp	Wet powder region
w	Water

Superscipts

′	Spatial derivative (variable per unit height) [m^{-1}]
-	Spatial average [–]

Yamane et al., 2003; Jones et al., 2022). However, they have neglected the potential effects that wetting-induced collapse of the powder bed could have on the characteristics of an inadvertent nuclear criticality excursion. The proposed mathematical and computational models in this research provide a means of simulating a wetting-induced volumetric collapse of a fissile powder bed, which is constrained radially by a cylindrical vessel.

Water infiltration into initially unsaturated or partially saturated pores located interstitially between powder particles may introduce a volumetric collapse, otherwise known as slump of the powder bed. Phenomenologically, slumping occurs as pressure variations cause meta-stable powder bed structures to collapse into more dense and stable configurations (Barden et al., 1973). These pressure variations cause a surface force to act on individual powder particles, which is driven by the balance between cohesive forces of the molecules within the liquid and surface tension between the solid and liquid phase (Lawton et al., 1992). The balance of these forces is typically termed as capillarity or matric suction. The added force on powder particles ultimately leads to the shear failure of inter-granular contacts between the powder particles, resulting in slumping (Lawton et al., 1992).

In high porosity, meta-stable fissile powder beds, wetting-induced volumetric collapse may lead to a significant re-distribution of fissile material and moderator in the powder bed. The effect that this has on the neutron kinetics of the system is not well known. Measurements performed on a series of Source d'Irradiation à Libre Evolution Neutronique (SILENE) sub-critical, fissile powder, nuclear criticality experiments at the CEA (Commissariat à l'énergie atomique et aux énergies alternatives) Valduc nuclear studies facility in France, showed that UO_2 powder beds, which form high porosity configurations, are susceptible to significant volumetric collapse (Rozain et al., 1991). The low bulk density of UO_2 powders investigated by Dunn et al. (2013), supports the notion that UO_2 powders form meta-stable structures which may slump upon wetting.

Stack-slumping has been considered as an important phenomenon to understand for long-term geologic disposal of nuclear waste (Mason et al., 2012b). A study commissioned by the Nuclear Decommissioning Authority (NDA) used the FETCH, RTM and QSS codes (Mason et al., 2009), to investigate postulated post-closure nuclear criticality excursion scenarios resulting from stack slumping in deep geological disposal facilities (GDFs). These repositories were to consist of fissile waste packages stacked one on top of the other in a sub-critical configuration. The incursion of water into the repository may then remove packaging grout placed around the packages that contain fissile material. This led to structural instability of the fissile stacks, causing a slump to occur. In certain cases, the volumetric slump of the fissile waste may lead to a delayed or prompt critical configuration (Mason and Smith, 2015). Although this is not the type of collapse treated in this study, it highlights how delayed or prompt critical configurations may form from the compacting of fissile material.

Another phenomenon that involves coupled neutron kinetics and porous media fluid dynamics, similar to the models proposed in this paper, is the Oklo natural nuclear reactor that was known to operate two billion years ago. The Oklo natural nuclear reactor has been proposed as a natural analogue for post-closure nuclear criticality safety studies for deep GDFs (Mason et al., 2012a). The existence of such a reactor was first postulated by Kuroda (1956) and was shown to exist in Gabon by Francis Perrin, who, in 1972, examined mined uranium deposits with less ^{235}U than should currently exist in natural uranium (Gil, 2018). After physical examination of the Oklo site where the ore was mined, the presence of 16 lenticular zones interspersed within sandstone was found. Two billion years ago, when the natural enrichment levels of uranium ore were much higher ($\approx$ 3.7 %) (Bentridi et al., 2011), water infiltration through the porous sandstone, into the lenticular uranium deposits, led to cyclical transient nuclear criticality excursions which subsequently caused boiling and other nuclear thermal-hydraulic phenomena. A comprehensive review of the physics behind the Oklo natural nuclear reactor is provided by Naudet (1991). Ibekwe et al. (2020) re-produced the key features of the long-term and short-term behaviour of the Oklo natural nuclear reactor using similar techniques to the models proposed in this research, highlighting a potential future application for this type of modelling. The models may even be extended to investigate nuclear geyser phenomena, which are postulated to be driven by natural nuclear reactors (Ebisuzaki and Maruyama, 2017). These nuclear geysers are of specific interest as they have been postulated to be locations where the origins of life reside (Maruyama et al., 2019). This type of reactor may exhibit phenomenologically similar processes to the proposed model, whereby the infiltration of water into porous fissile material causes a transient nuclear criticality excursion, which then leads to a violent expulsion of superheated water into the atmosphere and other phenomena (Ebisuzaki and Maruyama, 2017).

Other occurrences of collapse phenomenon, introducing the potential for transient nuclear criticality excursions, have emerged from structurally unstable debris beds that have formed from reactor cores due to nuclear power plant accidents such as the Fukushima Daiichi disaster (Coindreau et al., 2013; Tuya and Obara, 2017). Debris beds have also been used as an approximate geometry for modelling re-criticality in damaged light water reactor (LWR) cores under re-flooding conditions, similar to the Three Mile Island nuclear criticality accident (Schwinkendorf, 1999). Boiling water reactors (BWRs) also pose a risk of re-flooding induced re-criticality under certain accident conditions (Frid et al., 2001). Geometrically, debris beds can be modelled in a similar way to fissile powder beds, by approximating the

system as an array of spherical fissile particulates immersed in water (Fukuda et al., 2021). Therefore, phenomenological similarities can also be made when modelling transient nuclear criticality excursions in debris beds to those in powder-based systems, potentially giving another application for the present research.

Core redistribution and compaction is a subject of interest for space nuclear safety applications, where postulated re-entry accidents may lead to severe geometric alterations to a space nuclear reactor (Marshall, 2008). Marshall (2008) uses a geometric and material buckling approximation for the neutron diffusion equation to estimate the change in the effective multiplication factor of a compacted and reshaped core. Other forms of compaction may occur in highly enriched fuel containers, containing fissile material dispersed in the air (or an alternative gas). The compaction of this type of container may cause an inadvertent nuclear criticality excursion by reducing neutron leakage. The proposed model of volumetric collapse due to wetting could be adapted to simulate a similar phenomenon, whereby the collapse is induced via solid–solid contact stress.

The governing equations used in this research are an extension of the coupled point neutron kinetics, water infiltration, spatial nuclear thermal hydraulics, spatial radiolytic gas and steam production models described in Jones et al. (2022). These models are applied to high porosity, meta-stable 5-wt% enriched UO_2 powder bed, contained within a cylindrical open-topped vessel, wetted from above due to the activation of a fire-sprinkler system. A combination of the water infiltration and the collapse of the fissile material into a more compact configuration initiates a transient nuclear criticality excursion. As previously mentioned, this type of transient nuclear criticality excursion has been proposed in the research literature (Doucet et al., 2003; Sakai et al., 2004; Duhamel et al., 2004; IAEA, 2014). The characteristics of transient nuclear criticality excursions caused by differing rates of wetting-induced volumetric collapse are investigated in this study.

2. Existing point neutron kinetics model with associated nuclear thermal hydraulics, radiolytic gas and steam production equations

2.1. The governing equations for the mathematical model

The neutron kinetics equations previously defined by numerous authors have been used to model the neutron kinetics of the wetted fissile powder (Duderstadt and Hamilton, 1976; Stacey, 2018). Certain governing equations used to describe the nuclear thermal hydraulics, radiolytic gas generation and steam production are similar to those outlined in Jones et al. (2022) and are summarised here as:

$$\frac{dn(t)}{dt} = \frac{\beta_{\text{eff}} n(t)}{\Lambda}\left(R_{\text{T}}(t) - 1\right) + \sum_{\text{i}=1}^{6} \lambda_{\text{i}} C_{\text{i}}(t) + s_{\text{n}} \tag{1}$$

$$\frac{dC_{\text{i}}(t)}{dt} = -\lambda_{\text{i}} C_{\text{i}}(t) + \frac{\beta_{\text{i}}}{\Lambda} n(t) \tag{2}$$

$$M'_{\text{p,dp}} c_{\text{p}} \frac{\partial T_{\text{p,dp}}(t,z)}{\partial t} = E'_{\text{gen,p}}(t,z) + \frac{\partial}{\partial z}\left(\kappa_{\text{p}}(T_{\text{p,dp}}) v_{\text{f,p,dp}} \pi R^2 \frac{\partial T_{\text{p,dp}}(t,z)}{\partial z}\right) \tag{3}$$

$$\begin{aligned} c_{\text{w}}\left[\frac{\partial}{\partial t}\left(M'_{\text{w,wp}}(t,z) T_{\text{w,wp}}(t,z)\right) + \frac{\partial}{\partial z}\left(M'_{\text{w,wp}}(t,z) U_{\text{w}}(t) T_{\text{w,wp}}(t,z)\right)\right] \\ = E'_{\text{gen,w}}(t,z) + \\ E'_{\text{convec}}(t,z) + \frac{\partial}{\partial z}\left[c_{\text{w}} D_{\text{t,wp}} \frac{\partial}{\partial z}\left(M'_{\text{w,wp}}(t,z) T_{\text{w,wp}}(t,z)\right)\right] \end{aligned} \tag{4}$$

$$\begin{aligned} \frac{\partial V'_{\text{v,wp}}(t,z)}{\partial t} &= \frac{E'_{\text{boil,p}}(t,z)}{\rho_{\text{v}} h_{\text{lv}}} \\ &+ \frac{\partial}{\partial z}\left(D_{\text{t,wp}} \frac{\partial V'_{\text{v,wp}}(t,z)}{\partial z} - \left(U_{\text{w}}(t) - U_{\text{g}}(t,z)\right) V'_{\text{v,wp}}(t,z)\right) \end{aligned} \tag{5}$$

$$\begin{aligned} \frac{\partial V'_{\text{rg,wp}}(t,z)}{\partial t} &= (1-g_{\text{p}})(1 - v_{\text{f,g,wp}}(t,z)) G(\text{H}_2) P'(t,z) \\ &+ \frac{\partial}{\partial z}\left(D_{\text{t,wp}} \frac{\partial V'_{\text{rg,wp}}(t,z)}{\partial z} - \left(U_{\text{w}}(t) - U_{\text{g}}(t,z)\right) V'_{\text{rg,wp}}(t,z)\right) \end{aligned} \tag{6}$$

Eqs. (1) and (2) describe the rate of change of neutrons and delayed neutron precursors respectively within the wetted fissile powder system. Eqs. (3) and (4) respectively describe the nuclear thermal hydraulics of the dry powder bed and pore water. Eqs. (5) and (6) describe the spatial rate of change of steam and radiolytic gas products in the pores.

2.2. Supplementary equations

Supplementary equations used to quantify all parameters described in Eqs. (1) to (6) have been described in detail within Jones et al. (2022) and are summarised in Eqs. (7) to (30).

$$\begin{aligned} R_{\text{T}} = {} & R_{\text{imm}}(f_{\text{imm}}) + \Delta R_{\text{th,p,dp}}(\bar{T}_{\text{p,dp}}, f_{\text{imm}}) + \Delta R_{\text{th,p,wp}}(\bar{T}_{\text{p,wp}}, f_{\text{imm}}) \\ & + \Delta R_{\text{th,w,wp}}(\bar{T}_{\text{w,wp}}, f_{\text{imm}}) + \Delta R_{\text{void,wp}}(\bar{v}_{\text{f,g,wp}}, f_{\text{imm}}) \\ & + \Delta R_{\text{void,sus}}(\bar{v}_{\text{f,g,sus}}, f_{\text{imm}}) \end{aligned} \tag{7}$$

$$f_{\text{imm}}(t) = \frac{H_{\text{wp}}(t)}{H_{\text{dp}}(t) + H_{\text{wp}}(t)} \tag{8}$$

$$M'_{\text{p,dp}} = \rho_{\text{p,th}} \pi R^2 v_{\text{f,p,dp}} \tag{9}$$

$$M'_{\text{w,wp}}(t,z) = \rho_{\text{w,th}} \pi R^2 v_{\text{f,w,wp}}(t,z) \tag{10}$$

$$U_{\text{w}}(t) = \frac{K_{\text{sat,e}}(1 - \bar{v}_{\text{f,g,wp}}(t))}{\left(1 - v_{\text{f,p,wp}}\right) \Delta S_{\text{w}}} \left(\frac{H_{\text{sus}}(t) + h_{\psi} + H_{\text{wp}}(t)}{H_{\text{wp}}(t)}\right) \tag{11}$$

$$k = \frac{\left(1 - v_{\text{f,p,dp}}\right)^3}{5 S_{\text{A}}^2 v_{\text{f,p,dp}}^2} \tag{12}$$

$$K_{\text{sat,e}} = \frac{k \rho_{\text{w,th}} g}{2 \mu_{\text{w}}} \tag{13}$$

$$E'_{\text{gen,p}}(t,z) = (g_{\text{p}} + (1-g_{\text{p}}) v_{\text{f,g,wp}}(t,z)) P'(t,z) \tag{14}$$

$$E'_{\text{gen,w}}(t,z) = (1-g_{\text{p}})(1 - v_{\text{f,g,wp}}(t,z)) P'(t,z) \tag{15}$$

$$g_{\text{p}} = \begin{cases} \frac{3 d_p}{8 R_{\text{fiss}}} \; ; \; d_p < R_{\text{fiss}} \\ 1 - \frac{3 R_{\text{fiss}}}{4 d_p} + \frac{R_{\text{fiss}}^3}{8 d_p^3} \; ; \; d_p > R_{\text{fiss}} \end{cases} \tag{16}$$

$$P'(t,z) = E_{\text{f}} \int_0^{\infty} d E \, \Sigma_{\text{f}}(t,z,E) N(t) \hat{\phi}(z,E) V_n(E) \tag{17}$$

$$E'_{\text{convec}}(t,z) = h_{\text{p,w}}(t) v_{\text{f,w,wp}}(t,z) A'_{\text{p,w}}\left(T_{\text{p,wp}}(t,z) - T_{\text{w,wp}}(t,z)\right) \tag{18}$$

$$A'_{\text{p,w}} = \frac{6 \pi R^2 v_{\text{f,s,wp}}}{d_{\text{p}}} \tag{19}$$

$$h_{\text{p,w}}(t) = \frac{\kappa_{\text{w}}}{d_{\text{p}}}\left[2 + 1.1\left(\frac{c_{\text{w}} \mu_{\text{w}}}{\kappa_{\text{w}}}\right)^{1/3}\left(\frac{\rho_{\text{th,w}} U_{\text{w}}(t) d_{\text{p}}}{\mu_{\text{w}}}\right)^{0.6}\right] \tag{20}$$

$$E'_{\text{boil,p}}(t,z) = h_{\text{p,v}}(t,z) A'_{p,w}(t,z) v_{\text{f,w,wp}}(t,z) \max\left[0, \left(T_{\text{I}}(t,z) - T_{\text{sat}}\right)\right] \tag{21}$$

$$T_{\text{I}}(t,z) = \frac{1}{2}\left(T_{\text{p,wp}}(t,z) + T_{\text{w,wp}}(t,z)\right) \tag{22}$$

$$h_{\text{p,v}}(t,z) = 0.67\left[\frac{\lambda_{\text{v}}^3 \rho_{\text{v}} g (\rho_{\text{th,w}} - \rho_{\text{th,v}})\left(h_{\text{l,v}} + 0.4 c_{\text{v}}(T_{\text{I}}(t,z) - T_{\text{sat}})\right)}{\mu_{\text{v}} d_{\text{p}} (T_{\text{I}}(t,z) - T_{\text{sat}})}\right]^{0.25} \tag{23}$$

$$d_{\mathrm{b}}(t,z) = 1.0784\times10^{-2} v_{\mathrm{f,g}}(t,z)^{0.26}\left(\frac{\mu_{\mathrm{w,th}}}{\mu_{\mathrm{eff}}(t,z)}\right)^{-0.21}\left(\frac{\rho_{\mathrm{eff}}(t,z)}{\rho_{\mathrm{w,th}}}\right)^{-0.1} \quad (24)$$

$$U_{\mathrm{g}}(t,z) = \left(\frac{\sigma g}{\rho_{\mathrm{eff}}(t,z)}\right)^{0.25} \times\left[\left(\frac{\left(\frac{g\mu_{\mathrm{eff}}^4(t,z)}{\rho_{\mathrm{eff}}(t,z)\sigma^3}\right)^{-0.25}}{\max\left(K_{b,0}\left(\frac{g\mu_{\mathrm{eff}}^4(t,z)}{\rho_{\mathrm{eff}}(t,z)\sigma^3}\right)^{-0.038},12\right)}\left(\frac{d_{\mathrm{b}}^2\rho_{\mathrm{eff}}(t,z)g}{\sigma}\right)\right)^{-n_{\mathrm{c}}} + \left(\frac{2c\sigma^{0.5}}{d_{\mathrm{b}}(\rho_{\mathrm{eff}}(t,z)g)^{0.5}} + \left(\frac{d_{\mathrm{b}}(\rho_{\mathrm{eff}}(t,z)g)^{0.5}}{2\sigma^{0.5}}\right)\right)^{-0.5n_{\mathrm{c}}}\Bigg]^{-1/n_{\mathrm{c}}} \quad (25)$$

$$\rho_{\mathrm{eff}}(t,z) = \rho_{\mathrm{p,th}} v_{\mathrm{f,p}}(t,z) + \rho_{\mathrm{w,th}} v_{\mathrm{f,w}}(t,z) + \rho_{\mathrm{g,th}} v_{\mathrm{f,g}}(t,z) \quad (26)$$

$$\mu_{\mathrm{eff}}(t,z) = \mu_{\mathrm{w,th}} v_{\mathrm{f,w}}(t,z)^{-2.8} \quad (27)$$

$$v_{\mathrm{f,p}}(t,z) + v_{\mathrm{f,w}}(t,z) + v_{\mathrm{f,rg}}(t,z) + v_{\mathrm{f,v}}(t,z) = 1 \quad (28)$$

$$-\nabla\cdot D(\vec{r},E)\nabla\phi(\vec{r},E) + \Sigma_t(\vec{r},E)\phi(\vec{r},E) = \int_0^\infty dE'\,\Sigma_s(\vec{r},E'\rightarrow E)\phi(\vec{r},E') + \frac{\chi_{\mathrm{p}}(E)}{k_{\mathrm{eff}}}\int_0^\infty dE'\,\bar{\nu}\Sigma_f(\vec{r},E')\phi(\vec{r},E') \quad (29)$$

$$\hat{\phi}(z,E) = \frac{\int_0^R r\,dr\,\phi(r,z,E)}{\int_0^{H_{\mathrm{dp+wp+sus}}} dz\int_0^R r\,dr\int_0^\infty dE\,\phi(r,z,E)} \quad (30)$$

Eq. (7) represents the total reactivity of the wetted fissile powder due to the summation of various components. Eq. (8) represents the fraction of the powder bed that is wetted. Eqs. (9) and (10) are used to calculate the powder and pore water masses per unit height, respectively. Eq. (11) describes the forced advection speed of the water in the porous medium due to infiltration.

Eq. (12) is the Koseny–Carman equation used to describe the permeability of the porous medium and Eq. (13) is the effective saturated hydraulic conductivity of the powder bed. The applicability of the Koseny–Carman equation in modelling infiltration into UO_2 powder beds has been discussed for a very similar system in Jones et al. (2022). Therein the work of Odong (2007) is referred to, which shows that the Kozeny–Carman equation is applicable up to mean powder particle sizes, $d_{\mathrm{p}} = 300$ μm. Eqs. (14) and (15) represent the generation of thermal energy due to fission in the powder and surrounding water, respectively, with the energy deposition fraction of fission products described by Eq. (16). The linear power density, or fission power per unit height, is given by Eq. (17). The convective heat transfer rate per unit height is represented by Eq. (18) with the interfacial area per unit height and the convective heat transfer coefficient described by Eqs. (19) and (20) respectively. Boiling on the surface of powder particles is described by Eq. (21). The interface temperature between a powder particle and the surrounding water may be found using Eq. (22). The correlation used to describe the boiling heat transfer coefficient between the powder and vapour is shown in Eq. (23).

Correlations for the gas bubble size and gas bubble advective speed are respectively defined by Eqs. (24) and (25). Effective properties of the medium including the density and dynamics viscosity are outlined by Eqs. (26) and (27) respectively. Eq. (28) specifies the condition for the maximum volume fraction of the fissile powder bed based on the constituent components present.

Eq. (29) is the steady-state, multidimensional, multi-group, neutron diffusion equation (NDE). The NDE is a partial-integro-differential equation (PIDE) and also an approximation to the more accurate neutron transport equation (NTE) (Stacey, 2018). The NDE is a reasonable approximation to the NTE for neutron migration in weakly absorbing media several mean free paths away from any isolated sources, boundaries of the domain or at the interfaces between materials with significantly different material properties (Stacey, 2018).

For the mathematical model described in this article, the NDE is solved as an eigenvalue problem (for k_{eff}), at numerous snapshots in time (quasi-statically), in an azimuthally symmetric cylindrical coordinate system, to determine the radially averaged, energy-dependent scalar neutron flux distribution presented in Eq. (30). Solving the NDE using a quasi-static approach ensures that significant geometric variations to the system can be captured even when using the point neutron kinetics equations. Furthermore, the quasi-static neutron diffusion equation is solved every time the total reactivity, calculated using Eq. (7) varies by more than 0.5 $.

As this is a k_{eff} (or eigenvalue) nuclear criticality calculation, the scalar neutron flux may have an arbitrary normalisation (Stacey, 2018). Therefore, in practice, the radially-averaged scalar neutron flux is normalised such that the following is satisfied:

$$\int_0^{H_{\mathrm{dp+wp+sus}}} dz\int_0^\infty dE\,\hat{\phi}(z,E) = 1 \quad (31)$$

The quasi-steady state neutron diffusion equation is solved every time the total reactivity, calculated using Eq. (7) varies by more than 0.5 $. The separability of the amplitude and spatial components of the neutron fl

2.3. Prescribed boundary and interface conditions

Prescribed continuity conditions for each phase across the interface between the wet powder and pooled water regions are different from Jones et al. (2022) due to the effect that slumping has on the water and gas continuity equations.

Conditions are prescribed at the interface between the bottom of the dry powder and the base of the vessel such that no heat is transferred across the boundary:

$$\frac{\partial T_{\mathrm{p,dp}}(t,0)}{\partial z} = 0 \quad (32)$$

In the case where the bed is saturated no thermal energy exchange occurs across the bottom boundary:

$$\frac{\partial T_{\mathrm{p,wp}}(t,0)}{\partial z} = 0 \quad (33)$$

and:

$$\frac{\partial T_{\mathrm{w,wp}}(t,0)}{\partial z} = 0 \quad (34)$$

No exchange of steam or radiolytic gas occurs across the interface between the dry and wet powder regions with the following interface condition prescribed:

$$\frac{\partial V'_{\mathrm{rg,wp}}(t,H_{\mathrm{dp}})}{\partial z} = 0 \quad (35)$$

and:

$$\frac{\partial V'_{\mathrm{v,wp}}(t,H_{\mathrm{dp}})}{\partial z} = 0 \quad (36)$$

For the steady-state, multi-group, spatially-dependent, neutron diffusion equation (NDE), Eq. (29), vacuum boundary conditions are prescribed:

$$0 = \frac{1}{4}\phi(r,z) - \frac{1}{2}D(r,z)\frac{\partial}{\partial\vec{n}}\phi(r,z) \quad (37)$$

3. Extensions to the mathematical and phenomenological models

3.1. Extension to include powder bed slumping

Slumping occurs when there is an alteration to the pore-scale forces acting on the fissile powder bed. Susceptible powder beds are those that

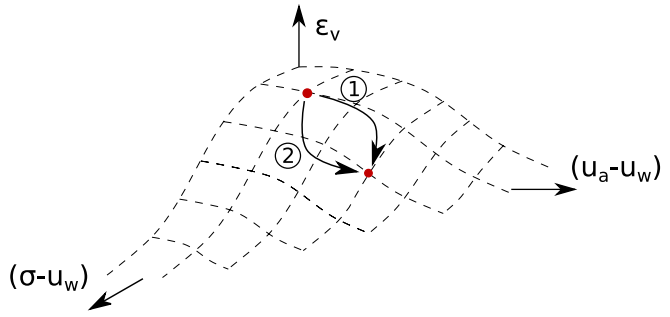

Fig. 1. A state surface for a given porous media collapse phenomenon indicating the initial and final states connected by lines 1 and 2 indicating various ways in which slumping may occur.
Source: Reproduction from Fredlund et al. (2012).

form meta-stable, low bulk density configurations. A comprehensive review of the different slumping mechanisms may be found in Al-Rawas (2000). Fredlund and Morgenstern (1976) introduced a framework for modelling volumetric slumping through the use of constitutive relations based upon the linearity of the stress–strain relationship for a powder bed. In this model, local variations in porosity are not considered. This approach has successfully been used by Pereira and Fredlund (2000), Li et al. (2016) and Houston et al. (1993) investigating slumping in porous media systems. Tadepalli and Fredlund (1991) showed that this solid mechanics model of porous bed slumping could be validated by experimental data. Rao and Revanasiddappa (2000) successfully used this methodology on porous media with wide range of mean particle sizes. This framework has also been applied by Cho and Lee (2001) and Sun et al. (2016) who simulated wetting-induced slumping of three-phase porous media.

In a fissile powder bed, two components of stress comprise this volumetric stress–strain relationship. The first arises as water percolates through the powder bed, where a balance of cohesive and adhesive forces between the water and powder particles alters the effective stress on powder particles (Bresson and Moran, 2004). This may lead to local shear failure between the powder grains, causing the powder bed to slump, forming a more dense configuration (Tadepalli et al., 1992). Swelling may also occur, whereby the fissile powder bed expands upon water infiltration (Fredlund and Morgenstern, 1976). The second component of stress occurs due to variations in axial pressure on the fissile powder bed from direct contact forces on the powder particles. Together, these factors form a stress–strain state surface which can be seen in Fig. 1. Here, a path from one state point to another identifies the volumetric changes experienced by the powder bed as a result of pressure variations. Typically, these state surface compression/expansion paths exhibit hysteresis, which is not considered in the present study (Fredlund et al., 2012). This work is concentrated solely on the wetting-induced component of slumping and how this affects a wetting-induced transient nuclear criticality excursion within a UO_2 powder bed.

The matric suction, ψ [Pa], may be defined as the difference between the pore-air, u_a [Pa] and pore-water, u_w [Pa] pressures:

$$\psi = u_a - u_w \tag{38}$$

The matric potential varies from its maximum value in the unsaturated region to zero in the saturated region (Brooks and Corey, 1964). Using a sharp wetting front model previously described by Jones et al. (2022), it follows that the matric potential behaves as a step function at the wetting front. Slumping caused by changes to the matric potential is therefore expected to occur as the dry fissile powder becomes wetted, not in the already wetted powder. The equation describing how alterations to the matric potential lead to volumetric strain in the wetted powder, denoted $\epsilon_v(t)$ [–], is (Fredlund and Morgenstern, 1976):

$$\epsilon_v(t) = \frac{1}{\pi R^2 U_w(t)} \frac{dV_{wp}(t)}{dt} = m_2^s \Delta\psi \tag{39}$$

where dV_{wp}/dt [$m^3\ s^{-1}$] represents the rate of volumetric deformation of the wetted powder and m_2^s [Pa^{-1}] is an empirically determined compressibility modulus describing the gradient of the powder bed effective stress–strain curve.

The fissile powder beds considered here are contained within cylindrical vessels which prevent radial expansion. This scheme, known as K_0 loading, yields the following relation for the compressibility modulus due to wetting (Fredlund et al., 2012):

$$m_2^s = \frac{1 + \nu_p}{E_\psi (1 - \nu_p)} \tag{40}$$

where E_ψ [Pa] is the modulus of elasticity for the powder bed with respect to changes in matric potential, and ν_p [–] is Poisson's ratio for the powder bed.

For a step change in matric potential across the wetting front, Eq. (39) may be written as:

$$U_{slump}(t) = U_w(t) m_2^s \Delta\psi \tag{41}$$

where $U_{slump}(t)$ [$m\ s^{-1}$] is the rate of collapse of the wet powder, pooled water interface.

Since the compressibility due to wetting, m_2^s and the change in matric potential across the wetting front, $\Delta\psi$ for a UO_2 powder bed is unknown, one may define a combined parameter which is varied to capture different levels of volumetric collapse. The slumping fraction, f_{slump} [–], due to wetting may then be defined as:

$$U_{slump}(t) = U_w(t) f_{slump} \tag{42}$$

3.2. Region height change equations for water infiltration and slumping

The following set of equations representing the time rate of change of each region may be found by combining infiltration and slumping processes:

$$\frac{dH_{dp}(t)}{dt} = -U_w(t) \tag{43}$$

$$\frac{dH_{wp}(t)}{dt} = U_w(t) - U_{slump}(t) \tag{44}$$

$$\frac{dH_{sus}(t)}{dt} = U_{w,in}(t) - \left(U_w(t) - U_{slump}(t)\right)\left(1 - v_{f,p,wp}\right)\Delta S_w \tag{45}$$

An additional component applies to Eq. (45) due to the generation of radiolytic gas and steam products from within the domain. This is accounted for by adjusting the height of the pooled water (free surface), by the net volumetric of flow of products per unit area, across the cell containing the pooled water interface. This is calculated using the volumetric flow gradients once the donor–acceptor scheme has been carried out throughout the domain (see Section 3.8 for further description). A corresponding representation of the three region sharp interface problem is presented in Fig. 2.

3.3. Continuous model of powder slumping and exchange across wetting front

The exchange of powder particles from the dry powder region to the wetted powder region is described by the following equation:

$$(U_w(t) - U_{slump}(t)) N'_{p,wp} = U_w(t) N'_{p,dp} \mathbf{H}(H_{dp}) \tag{46}$$

where $N'_{p,dp}$ and $N'_{p,wp}$ are the number of UO_2 powder particles per unit height present in the dry and settled wet powder regions, respectively. Here, $\mathbf{H}(H_{dp})$ is a Heaviside step function, introduced to adjust the boundary condition to one of no mass transfer when the bed is saturated, i.e. if $H_{dp} = 0$ m.

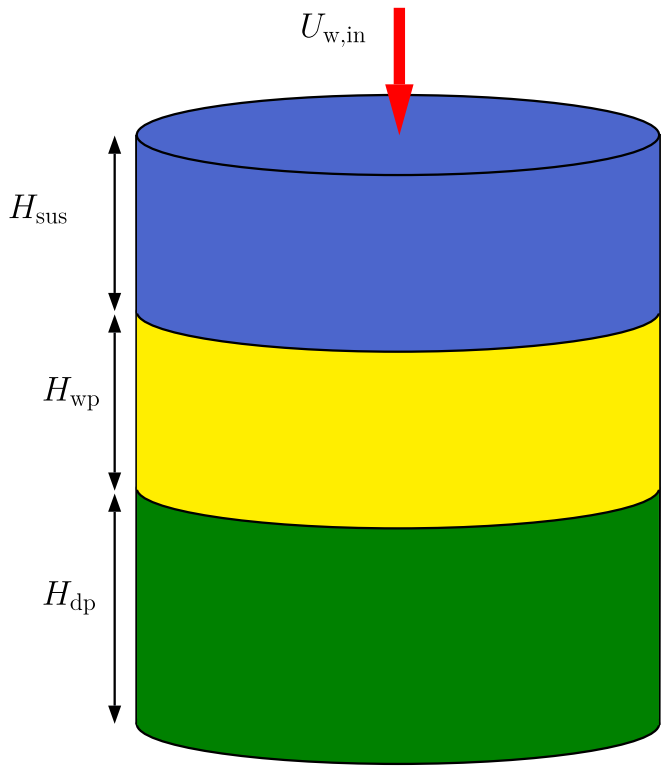

Fig. 2. A representation of the three region powder drum. The top blue region represents the pooled water on the surface of the powder. The middle yellow region corresponds to the homogeneous mixture of water and UO_2 powder. The bottom green region represents the dry UO_2 powder. The height of each interface may vary as a consequence of the described phenomenological processes in action.

Given that $U_{slump}(t) = U_w(t) f_{slump}$, Eq. (46) may be found to be spatially and temporally independent such that:

$$N'_{p,wp} = N'_{p,dp} \frac{1}{1 - f_{slump}} \tag{47}$$

3.4. Modelling water flow through porous medium and pooled water

The continuity equation for water present in the interstices of powder particles, denoted $V_{w,wp}(t,z)$ [m^3] consists of an advective infiltration term and a dispersive turbulent mixing term. A volumetric term also exists that reduces water volume in the case of boiling and radiolysis. This is expressed using the following equation:

$$\frac{\partial V'_{w,wp}(t,z)}{\partial t} = \frac{\partial}{\partial z}\left(-U_w(t)V'_{w,wp}(t,z)\mathbf{H}(H_{dp}) + D_{t,wp}\frac{\partial V'_{w,wp}(t,z)}{\partial z}\right) - \frac{E'_{boil,p}(t,z)}{\rho_{w,th}h_{l,v}} - (1-g_p)(1-v_{f,g,wp}(t,z))G(H_2)P'(t,z) \tag{48}$$

Water percolating through the powder bed causes the wetting front to infiltrate the dry powder region. This may be described using the interface flux condition in Eq. (49), which states that the dispersion across the interface is zero. Upwind spatial differencing of the advective term in Eq. (48) means that water is added to the discretised horizontal slice adjacent to the interface, thus moving the interface:

$$D_{t,wp}\frac{\partial V'_{w,wp}(t,H_{dp})}{\partial z} = 0 \tag{49}$$

In the pooled water region, the continuity equation consists of an advective infiltration term and a dispersive turbulent mixing term. The advective term is now comprised of both infiltration and slumping components such that:

$$U_{w,sus}(t) = U_w(t)\left(1 - v_{f,p,wp}\right)\Delta S_w + U_{slump}(t)v_{f,p,wp} \tag{50}$$

This then yields the following continuity equation for the pooled water:

$$\frac{\partial V'_{w,sus}(t,z)}{\partial t} = \frac{\partial}{\partial z}\left[-U_{w,sus}(t)V'_{w,sus}(t,z)\mathbf{H}(H_{dp}) + D_{sus}\frac{\partial V'_{w,sus}(t,z)}{\partial z}\right] \tag{51}$$

At the interface between the pore and pooled water, there is a flux balance which results in the movement of water held in the pores to the pooled water at a rate corresponding to the rate of slumping, such that the following is satisfied:

$$-U_w(t)V'_{w,wp}(t,H_{dp+wp})\mathbf{H}(H_{dp}) + D_{wp}\frac{\partial V'_{w,wp}(t,H_{dp+wp})}{\partial z} = -\left(U_{w,sus}(t) - U_{slump}(t)\right)V'_{w,sus}(t,H_{dp+wp})\mathbf{H}(H_{dp}) + D_{sus}\frac{\partial V'_{w,sus}(t,H_{dp+wp})}{\partial z} \tag{52}$$

The boundary condition, prescribed at the upper surface of the pooled water corresponds to a constant in-flux as water enters the domain at rate, $U_{w,in}$ [m s^{-1}]. This is described by:

$$-U_{w,sus}(t)V'_{w,sus}(t,H_{dp+wp+sus})\mathbf{H}(H_{dp}) + D_{sus}\frac{\partial V'_{w,sus}(t,H_{dp+wp+sus})}{\partial z} = -U_{w,in}\pi R^2\mathbf{H}(H - H_{dp+wp+sus}) \tag{53}$$

where H [m] is the total drum height. The condition $\mathbf{H}(H - H_{dp+wp+sus})$ ensures that when the powder drum is full, water is prevented from entering. Water and gas is removed from the upper surface when gasses created in the system cause the contents of the vessel to go above its maximum volume, $V = H\pi R^2$. No UO_2 powder is removed, since the present model does not consider the suspension of the powder from the settled wet powder bed.

3.5. Radiolytic gas and steam governing equations in the pooled water region

The governing equations corresponding to the generation, advection and mixing of radiolytic gas products (H_2) and steam are based on the work of Jones et al. (2022). Alterations are made here to model the gas velocity relative to the water velocity, and also to account for how slumping of the wetted powder bed affects the advection of gas through pores and in the pooled water. As such the continuity equations for radiolytic gas and steam in the pooled water are given respectively by:

$$\frac{\partial V'_{rg,sus}(t,z)}{\partial t} = \frac{\partial}{\partial z}\left(-\left(U_{w,sus}(t) - U_g(t,z)\right)V'_{rg,sus}(t,z) + D_{t,sus}\frac{\partial V'_{rg,sus}(t,z)}{\partial z}\right) \tag{54}$$

and:

$$\frac{\partial V'_{v,sus}(t,z)}{\partial t} = \frac{\partial}{\partial z}\left(-\left(U_{w,sus}(t) - U_g(t,z)\right)V'_{v,sus}(t,z) + D_{t,sus}\frac{\partial V'_{v,sus}(t,z)}{\partial z}\right) \tag{55}$$

The conservation of mass across the interface between the wet powder and pooled water regions is obtained through prescribing the following interface conditions:

$$-\left(U_w(t) - U_g(t,H_{dp+wp})\right)V'_{rg,wp}(t,H_{dp+wp}) + D_{t,wp}\frac{\partial V'_{rg,wp}(t,H_{dp+wp})}{\partial z} = -\left(U_{w,sus}(t) - U_g(t,H_{dp+wp}) - U_{slump}(t)\right)V'_{rg,sus}(t,H_{dp+wp}) + D_{t,sus}\frac{\partial V'_{rg,sus}(t,H_{dp+wp})}{\partial z} \tag{56}$$

and:

$$-\left(U_{\mathrm{w}}(t)-U_{\mathrm{g}}(t,H_{\mathrm{dp+wp}})\right)V'_{\mathrm{v,wp}}(t,H_{\mathrm{dp+wp}})+D_{\mathrm{t,wp}}\frac{\partial V'_{\mathrm{v,wp}}(t,H_{\mathrm{dp+wp}})}{\partial z}=-\left(U_{\mathrm{w,sus}}(t)-U_{\mathrm{g}}(t,H_{\mathrm{dp+wp}})-U_{\mathrm{slump}}(t)\right)V'_{\mathrm{v,sus}}(t,H_{\mathrm{dp+wp}})+D_{\mathrm{t,sus}}\frac{\partial V'_{\mathrm{v,sus}}(t,H_{\mathrm{dp+wp}})}{\partial z} \tag{57}$$

3.6. Nuclear thermal hydraulics in slumping wetted powder region and pooled water

Interphase thermal energy exchange, through processes such as boiling and convection, exist in the wetted powder region. A thermal energy source term is also present due to fission energy deposited in the wetted powder. Additionally, there is heat conduction between UO_2 powder particles. These processes have previously been described by Jones et al. (2022). An additional process may be included in the continuity equation that models thermal advection due to the volumetric collapse of the powder bed. The governing equation may then be formulated as:

$$M'_{\mathrm{p,wp}}c_{\mathrm{p}}\left[\frac{\partial T_{\mathrm{p,wp}}(t,z)}{\partial t}+\frac{\partial}{\partial z}\left(U_{\mathrm{slump}}(t)T_{\mathrm{p,wp}}(t,z)\right)\right]=E'_{\mathrm{gen,p}}(t,z)-E'_{\mathrm{convec}}(t,z)-E'_{\mathrm{boil,p}}(t,z)+\frac{\partial}{\partial z}\left(\kappa_{\mathrm{p}}(T_{\mathrm{p,wp}})\upsilon_{\mathrm{f,p,wp}}\pi R^2\frac{\partial T_{\mathrm{p,wp}}(t,z)}{\partial z}\right) \tag{58}$$

where $M'_{\mathrm{p,wp}}$ [kg m^{-1}] is the wetted powder mass per unit height, defined as:

$$M'_{\mathrm{p,wp}}=\rho_{\mathrm{p,th}}\pi R^2\upsilon_{\mathrm{f,p,wp}} \tag{59}$$

At the interface between the dry and wet powder region, the thermal energy flux between each region must balance for conservation. Therefore, this yields the following equation:

$$-M'_{\mathrm{p,wp}}c_{\mathrm{p}}(U_{\mathrm{w}}(t)-U_{\mathrm{slump}}(t))T_{\mathrm{p,wp}}(t,H_{\mathrm{dp}})+\kappa_{\mathrm{p}}(T_{\mathrm{p,wp}})\upsilon_{\mathrm{f,p,wp}}\pi R^2\frac{\partial T_{\mathrm{p,wp}}(t,H_{\mathrm{dp}})}{\partial z}=-M'_{\mathrm{p,dp}}c_{\mathrm{p}}U_{\mathrm{w}}(t)T_{\mathrm{p,dp}}(t,H_{\mathrm{dp}})+\kappa_{\mathrm{p}}(T_{\mathrm{p,dp}})\upsilon_{\mathrm{f,p,dp}}\pi R^2\frac{\partial T_{\mathrm{p,dp}}(t,H_{\mathrm{dp}})}{\partial z} \tag{60}$$

Continuity of thermal energy in the pooled water is given by the following equation:

$$c_{\mathrm{w}}\left[\frac{\partial}{\partial t}\left(M'_{\mathrm{w,sus}}(t,z)T_{\mathrm{w,sus}}(t,z)\right)+\frac{\partial}{\partial z}\left(M'_{\mathrm{w,sus}}(t,z)U_{\mathrm{w,sus}}(t)T_{\mathrm{w,sus}}(t,z)\right)\right]=\frac{\partial}{\partial z}\left[c_{\mathrm{w}}D_{\mathrm{t,sus}}\frac{\partial}{\partial z}\left(M'_{\mathrm{w,sus}}(t,z)T_{\mathrm{w,sus}}(t,z)\right)\right] \tag{61}$$

where the mass of water in the pooled water region per unit height, given by $M'_{\mathrm{w,sus}}$ [kg m^{-1}] is:

$$M'_{\mathrm{w,sus}}(t,z)=\rho_{\mathrm{w,th}}\pi R^2\upsilon_{\mathrm{f,w,sus}}(t,z) \tag{62}$$

The associated interface condition for the conservation of thermal flux across the boundary is defined as:

$$-M'_{\mathrm{w,wp}}(t,H_{\mathrm{dp+wp}})U_{\mathrm{w}}(t)T_{\mathrm{w,wp}}(t,H_{\mathrm{dp+wp}})+D_{\mathrm{t,wp}}\frac{\partial}{\partial z}\left(M'_{\mathrm{w,wp}}(t,H_{\mathrm{dp+wp}})T_{\mathrm{w,wp}}(t,H_{\mathrm{dp+wp}})\right)=-M'_{\mathrm{w,sus}}(t,H_{\mathrm{dp+wp}})\left(U_{\mathrm{w,sus}}(t)-U_{\mathrm{slump}}(t)\right)T_{\mathrm{w,sus}}(t,H_{\mathrm{dp+wp}})+D_{\mathrm{t,sus}}\frac{\partial}{\partial z}\left(M'_{\mathrm{w,sus}}(t,H_{\mathrm{dp+wp}})T_{\mathrm{w,sus}}(t,H_{\mathrm{dp+wp}})\right) \tag{63}$$

At the top of the domain, thermal energy enters the system at a given rate and temperature, satisfying the following equation:

$$-M'_{\mathrm{w,wp}}(t,H_{\mathrm{dp+wp+sus}})U_{\mathrm{w,sus}}(t)T_{\mathrm{w,sus}}(t,H_{\mathrm{dp+wp+sus}})+D_{\mathrm{t,sus}}\frac{\partial T_{\mathrm{w,sus}}(t,H_{\mathrm{dp+wp+sus}})}{\partial z}=-\rho_{\mathrm{w,th}}\pi R^2U_{\mathrm{w,in}}T_{\mathrm{w,in}} \tag{64}$$

3.7. Pressure drop through porous bed

The method outlined originally by Green and Ampt (1911), used to model water infiltration into porous media, assumes a laminar Darcian type flow, driven solely by hydrostatic head (Marsily, 1986). This has been successfully applied by Jones et al. (2022) to predict infiltration rates into low-enriched UO_2 powder beds. Other components of pressure that otherwise contribute to flow are not directly modelled. Furthermore, the flow is assumed to be incompressible, implying that continuous phase local pressure variations introduced by phenomenon such as shocks are neglected. A simple relation for hydrostatic head in the present model employs a homogenisation approach for calculating effective densities of the water and gas phases present. Furthermore, the dispersed gas bubbles are assumed to be in a pressure equilibrium with the surrounding continuous phase liquid. The resulting gauge pressure, taking the top of the pooled water as reference point, may be determined using the following expression:

$$P_{\mathrm{gauge}}(t,z)=\int_z^{H_{\mathrm{dp+wp+sus}}}\left(\rho_{\mathrm{w,th}}\frac{V'_{\mathrm{w}}(t,z)}{V'_{\mathrm{w}}(t,z)+V'_{\mathrm{g}}(t,z)}+\rho_{\mathrm{g,th}}\frac{V'_{\mathrm{g}}(t,z)}{V'_{\mathrm{w}}(t,z)+V'_{\mathrm{g}}(t,z)}\right)g\,dz \tag{65}$$

also:

$$P_{\mathrm{abs}}(t,z)=P_{\mathrm{atm}}+P_{\mathrm{gauge}}(t,z) \tag{66}$$

High pressure nucleating gas bubbles grow in the continuous liquid phase, exerting a surface force on the surrounding liquid, and thus displacing it. The amount of displacement that occurs depends primarily on the difference in pressure and dissolved concentration between the gas bubble and surrounding liquid (Lane et al., 1958). At present, the gas bubble size is modelled using the approach outlined by Zeitoun et al. (1994) and bubbles are assumed to nucleate instantaneously. Furthermore, the pressure inside gas bubbles are assumed to be in equilibrium with the surrounding continuous phase. This condition has been previously proposed by Yeoh and Tu (2019). In the case where large volumes of gas are produced rapidly, significant volumes of water and gas are forced upwards. Corresponding inter-phase pressure and force variations are accounted for by the turbulent mixing terms, $D_{\mathrm{t,wp}}$ and $D_{\mathrm{t,sus}}$.

3.8. Spatial discretisation, time-dependent solution algorithm and inter-phase coupling

A radially and azimuthally symmetric finite volume spatial discretisation scheme was employed using cylindrical co-ordinates. The dispersive and diffusive terms were discretised using second-order accurate spatial discretisation schemes. However, the advective terms in the governing PDE's were discretised using a first-order accurate upwind spatial discretisation scheme. A representation of the three region cylindrical domain is presented in Fig. 2.

The three sharp interfaces present in the problem are used to create cut-cells on a static one-dimensional cylindrical mesh. Inter-region mass fluxes may then be calculated across cut-cells to describe the flow of each phase around the cut-cell. A cell split-and-merge technique, such as the one described by Ingram et al. (2003), has been implemented to ensure that the Courant–Friedrichs–Lewy (CFL) condition and stability

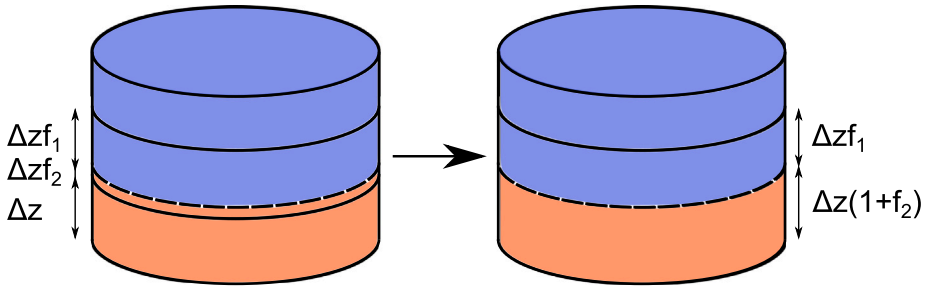

Fig. 3. Solid lines enclose mesh cells, the dashed line represents the region interface. The cut-cell method splits the cell containing the interface into two sub-cells. The cut-cell is merged with the adjacent cell when the minimum cut-cell height criterion is satisfied.

are maintained as the region interface approaches the static mesh cell boundary (Courant et al., 1928). A graphical representation of a cut-cell containing a region interface is presented in Fig. 3. Here, the variables f_1 and f_2 correspond to the fill fractions of a cell of height, Δz, by each region.

Using the cut-cell method, the explicit time integrator can maintain a similar step size to if there were no cut-cells (Ingram et al., 2003). A cut-cell is merged with an adjacent mesh cell when the following criterion is satisfied:

$$f_{1/2}\Delta z < 0.4\Delta z \tag{67}$$

The solution in time is found through an ODE solver created by Shampine and Gordon (1975) which uses a modified divided difference form of the Adams predict-evaluate–correct-evaluate (PECE) formula as well as local extrapolation. Absolute and relative error tolerances, denoted e_{abs} and e_{rel} respectively, are both prescribed $e_{\text{abs}} = e_{\text{rel}} = 10^{-7}$. These error tolerances are dynamically relaxed by the solution algorithm if the computation is not possible within the prescribed error tolerance.

The proposed model assumes that the flow of each phase is incompressible and one-dimensional. The rate of advection of each phase across a given control volume face is evaluated using prescribed empirical correlations. The effect that gas bubble nucleation and growth has on the rate of the continuous phase mass transfer is neglected in the governing equations. This may lead to an occasion whereby there are more products entering or leaving a control volume than is physical. Typically, for computational fluid dynamics (CFD) simulations, the inter-phase coupling, that affects the transport of each constituent phase, is modelled mathematically by adding relevant source terms to the Navier–Stokes momentum equations (Yeoh and Tu, 2019). Karema and Lo (1999) highlight how this may be carried out using a variety of different numerical techniques.

However, in the present study, the velocity of each phase and the inter-phase physics are captured through the use of empirical correlations, eliminating the need to solve the momentum equation. Although this requires an alternative way of achieving inter-phase coupling, it reduces the computational complexity of the problem whilst still capturing the phenomenological processes that are present. To prevent more products entering a cell than is physical, a donor–acceptor type scheme, similar to the methods in Hirt and Nichols (1981) is used. Here, information from the downwind cell in the upwind differencing scheme is used to ensure that the following multiphase incompressibility condition is satisfied (Kleinstreuer, 2003):

$$\nabla \cdot \left(\sum_{k=1}^{N_{\text{comp}}} \upsilon_{\text{f,k}} U_{\text{k}} \right) = 0 \tag{68}$$

where N_{comp} is the number of components modelled, $\upsilon_{\text{f,k}}$ is the volume fraction of each component and U_{k} is the rate of transfer of component, k, across each face of the control volume, including advection, dispersion and also the effects of source terms (such as boiling) within the control volume.

The methodology applied here involves sweeping through the domain from the bottom cell, containing the wetting front, to the free surface of the pooled water at the top of the domain. The total exchange between a given cell and the cell above may be described by the net volumetric exchange of products across the face. In a donor–acceptor cell scheme, the donor cell corresponds to the upwind cell, whereas the acceptor cell is downwind. The net flow of products across intermediate cell faces is then calculated as:

$$\frac{d\theta_{\text{D}}}{dt} = \frac{d\theta_{\text{rg,D}}}{dt} + \frac{d\theta_{\text{v,D}}}{dt} + \frac{d\theta_{\text{w,D}}}{dt} \tag{69}$$

where θ may represent either thermal energy or volume and the subscript, D, corresponds to the donor cell.

To ensure continuity and to satisfy the incompressible flow condition throughout the domain (Eq. (68)), the donor cell component temporal gradients are adjusted by exchanging products from the downwind acceptor cell, back into the donor cell. This results in the following adjustment:

$$\frac{d\theta_{\text{k,D}}}{dt} = \frac{d\theta_{\text{k,D}}}{dt} + \tilde{\upsilon}_{\text{f,k,A}} \frac{d\theta_{\text{D}}}{dt} \tag{70}$$

where the subscript, k may refer to the water, radiolytic gas or steam, and the subscript, A, refers to the acceptor cell. To ensure homogeneous dry and wet powder region powder bulk densities, the powder is not included in this adjustment. As such, the volume fractions of each component are re-calculated such that:

$$\tilde{\upsilon}_{\text{f,k}} = \frac{\upsilon_{\text{f,k}}}{\upsilon_{\text{f,w}} + \upsilon_{\text{f,rg}} + \upsilon_{\text{f,v}}} \tag{71}$$

where the subscript, k, may refer to the water, radiolytic gas or steam components.

On interfaces and boundaries, the appropriate condition governing the net flow rate of each component is satisfied by letting the total divergence of the flow across the face equal to the boundary/interface prescribed net rate of transfer across the face. A similar procedure using the donor/acceptor scheme may then be performed, ensuring the following condition remains satisfied:

$$\upsilon_{\text{f,w}} + \upsilon_{\text{f,rg}} + \upsilon_{\text{f,v}} + \upsilon_{\text{f,p}} = 1 \tag{72}$$

Once the adjustments to the net rate of flow of each component has been made throughout the domain, any non-zero volumetric gradient across the cell containing the pooled water interface causes the interface itself is moved. This is achieved by altering Eq. (45).

4. Properties of UO_2 powder bed undergoing wetting-induced collapse

The physical system examined in this paper is concerned with an initially dry powder bed which undergoes wetting from the top. Water entering the system percolates through the powder and also begins to pool on the surface of the powder bed. This adds reactivity to the system, resulting in a transient nuclear criticality excursion. Wetting of the powder bed also leads to a wetting-induced volumetric collapse

Table 1
Properties of the UO_2 powder bed, water, radiolytic gas (H_2) and steam.

Property	Symbol	Value
Specific heat capacity of UO_2	c_p	274 J kg^{-1} K^{-1}
Specific heat capacity of steam	c_v	2.060×10^3 J kg^{-1} K^{-1}
Specific heat capacity of water	c_w	4.2×10^3 J kg^{-1} K^{-1}
Pore water turbulent mixing coefficient	$D_{t,sus}$	10^{-3} m^2 s^{-1}
Pore water turbulent mixing coefficient	$D_{t,wp}$	10^{-4} m^2 s^{-1}
Pore water turbulent mixing coefficient	$D_{t,wp}$	10^{-4} m^2 s^{-1}
Energy generated per fission event	E_f	3.2×10^{-11} J fission^{-1}
Volumetric H_2 generation coefficient at STP	$G(H_2)$	5.36777×10^{-9} m^3 J^{-1}
Latent heat of vaporisation	$h_{l,v}$	2.2512×10^6 J kg^{-1}
Mean fission fragment range	R_0	7 μm
Intrinsic neutron source density	s_n	0.135 neutrons s^{-1} (cm^{-3} · UO_2)
Boiling point of water	T_{sat}	373.15 K
Water impinging rate from fire sprinkler	$U_{w,in}$	0.5 L s^{-1}
Fast prompt neutron speed	$V_n(E_{fast})$	1.4×10^9 cm s^{-1}
Thermal prompt neutron speed	$V_n(E_{therm})$	2.0×10^5 cm s^{-1}
Total effective delayed neutron fraction	β_{eff}	733×10^{-5}
Thermal expansion coefficient of water	η	2.14×10^{-4} K^{-1}
Mean neutron generation time	Λ	5.32959×10^{-5} s
Thermal conductivity of UO_2	κ_p	see Eq. (73)
Thermal conductivity of steam	κ_v	2.46×10^{-2} W m^{-1} K^{-1}
Dynamic viscosity of steam	μ_v	1.271×10^{-5} Pa s
Dynamic viscosity of water	μ_w	1.0×10^{-3} Pa s
Density of UO_2	$\rho_{p,th}$	10950 kg m^{-3}
Density of steam	$\rho_{v,th}$	5.863×10^{-1} kg m^{-3}
Density of water	$\rho_{w,th}$	998.1 kg m^{-3}

Table 2
Effective delayed neutron precursor group data.

Group, i	β_i ($\times 10^{-5}$)	λ_i (s)
1	25 ± 1	0.01335 ± 0.00000
2	129 ± 4	0.03264 ± 0.00000
3	122 ± 3	0.12099 ± 0.00000
4	279 ± 5	0.30482 ± 0.00001
5	125 ± 4	0.85704 ± 0.00003
6	53 ± 2	2.87888 ± 0.00015

of pore spaces between powder particles, resulting in a more tightly packed UO_2 powder configuration. The proposed model of collapse is investigated, with specific focus on how this phenomenon may affect the neutron kinetics of the dispersed powder–water–gas mixture.

4.1. Previously defined system properties

Many thermophysical and other properties of the UO_2 powder bed have been previously collated by Jones et al. (2022) and are summarised in Tables 1 and 2.

The point neutron kinetics parameters, such as the mean neutron generation time, effective delayed neutron fractions and decay constants, have been determined by MCNP using an adjoint flux weighting technique, as described by Kiedrowski et al. (2011). Bell and Glasstone (1970) notes that these properties typically vary as a function of time. In the proposed model, the neutron kinetic parameters will vary as the geometric properties of the system vary. Jones et al. (2022) examined a range of different bed immersion fractions for a very similar wetted UO_2 powder bed to that which has been modelled in this study. It was found that the adjoint weighted neutron kinetic properties did not vary widely as a function of the bed immersion fraction, therefore, a simple unweighted average value was used.

The thermal conductivity of the UO_2 powder is calculated using Eq. (73), from Fink et al. (1981).

$$\kappa_p = \left[0.068337 + 1.6693 \times 10^{-4} T_p + 3.1886 \times 10^{-8} T_p^2\right]^{-1} + 0.12783 T_p e^{-1.1608/k_b T_p} \quad (73)$$

where $k_b = 8.6144 \times 10^{-5}$ eV K^{-1} is the Boltzmann constant.

4.2. Variable system properties

4.2.1. Mean powder particle size

A nominal mean powder particle size of $d_p = 30$ μm has been chosen for the physical system studied in this paper. Sensitivity analysis is performed by increasing the particle size to $d_p = 100$ μm and examining the consequence this has on the volumetric slumping of the powder bed. The study also examines the effect that particle size and slumping have on the transient nuclear criticality excursion.

4.2.2. Wetting-induced slumping parameter

For the UO_2 powder system under consideration, both the compressibility modulus due to wetting (m_2^s) and the change in matric suction across the wetting front ($\Delta\psi$) are unknown. Therefore, these quantities have been combined in the proposed model into a term that represents the fractional slumping of newly wetted powder, denoted f_{slump}. Physically, the term f_{slump} represents the extent to which the pressure exchange across the wetting front, due to certain change matric potential, will cause a deformation of the powder bed proportional to the rate of water infiltration. The term is defined as:

$$f_{slump} = m_2^s \Delta\psi \quad (74)$$

The fractional slumping of newly wetted powder is varied from 0 to 0.6 for both powder beds considered in this work.

4.3. Steady-state scalar neutron flux spatial and energy distribution

Group condensed macroscopic neutron cross-sections were evaluated in each cell to consider the heterogeneity introduced into the system by having a spatially varying powder particle number density. This approach ensures that cells that contain no fissile material have zero macroscopic neutron fission cross-section. The functional dependence between the macroscopic neutron cross-sections and the porosity of an axial mesh cell was determined by performing a number of Serpent Monte Carlo neutron transport simulations (Leppänen et al., 2015). These simulations modelled a single spherical UO_2 powder particle contained within a cube of water, with the cube volume corresponding to a specific porosity, with reflective boundary conditions applied at the bounds of the cube. This models an infinite lattice of regularly spaced UO_2 powder particles. Fig. 4 shows a series of Serpent mesh plots for a powder particle, sized $d_p = 30$ μm, surrounded by a volume of water calculated to ensure a prescribed porosity.

Two-group condensed macroscopic neutron cross-sections were calculated from the point-wise continuous energy Monte Carlo neutron transport code Serpent using the geometries presented in Fig. 4 (Leppänen et al., 2015). The neutrons with energies below 0.625 eV were classified as thermal, whilst neutrons with energies above this threshold were classified as fast. Furthermore, all prompt neutrons born through fission are assumed to be fast such that $\chi_p(E_{fast}) = 1$ and $\chi_p(E_{therm}) = 0$. The resulting two-group macroscopic neutron cross-sections are shown as a function of bed porosity in Fig. 5. Small error bars indicate the low variance in the Serpent Monte Carlo neutron transport simulation results. A greater dependence on porosity can be seen for the thermal macroscopic neutron cross-sections than the fast macroscopic neutron cross-sections. Furthermore, within energy group macroscopic neutron scattering cross-sections are a stronger function of porosity than inter-group macroscopic neutron scattering cross-sections. Correlations of the general form described by Eq. (75), with coefficients listed in Table 3, provide an accurate representation of how these macroscopic neutron cross-sections vary as a function of powder bed porosity. The best-fit lines in Fig. 5 generated using these correlated macroscopic neutron cross-sections supports this.

$$\Sigma_{i,g} = C_0 + C_1(1 - v_{f,p}(t)) + C_2(1 - v_{f,p}(t))^2 \quad (75)$$

where i in $\Sigma_{i,g}$ [cm^{-1}] describes a specific macroscopic neutron reaction cross-section and subscript g refers to the specific, discretised energy group.

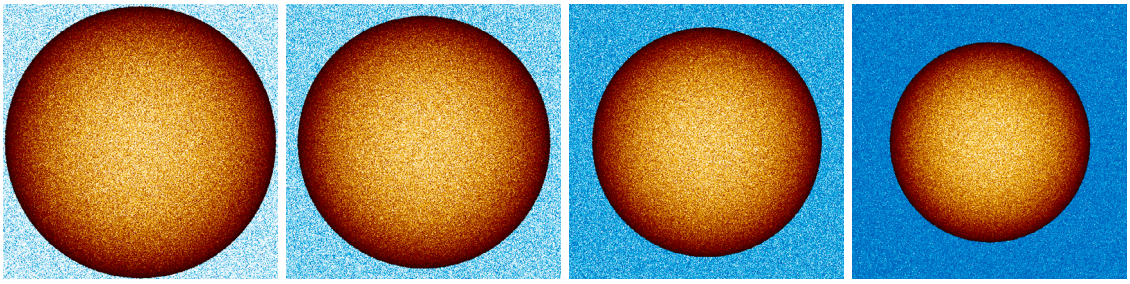

(a) $\epsilon_{\mathrm{wp}} = 0.5$ (b) $\epsilon_{\mathrm{wp}} = 0.6$ (c) $\epsilon_{\mathrm{wp}} = 0.7$ (d) $\epsilon_{\mathrm{wp}} = 0.8$

Fig. 4. Serpent representation of single UO_2 powder particle surrounded by a volume of water prescribed to ensure a specified domain porosity. Reflective boundary conditions model an infinite number of powder particles at the specified bed porosity.

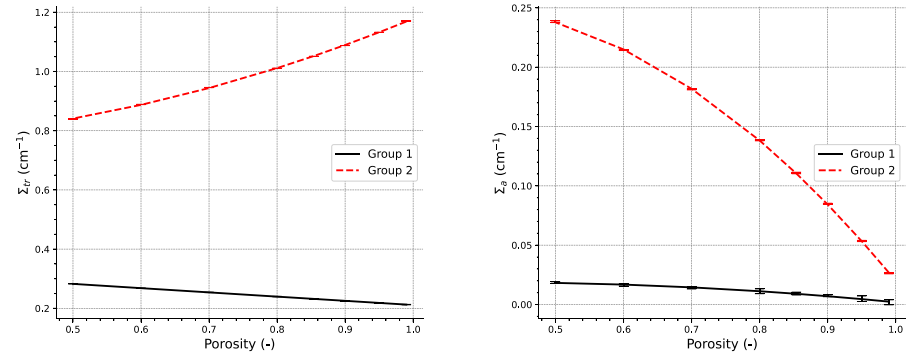

(a) Σ_{tr}. (b) Σ_{a}.

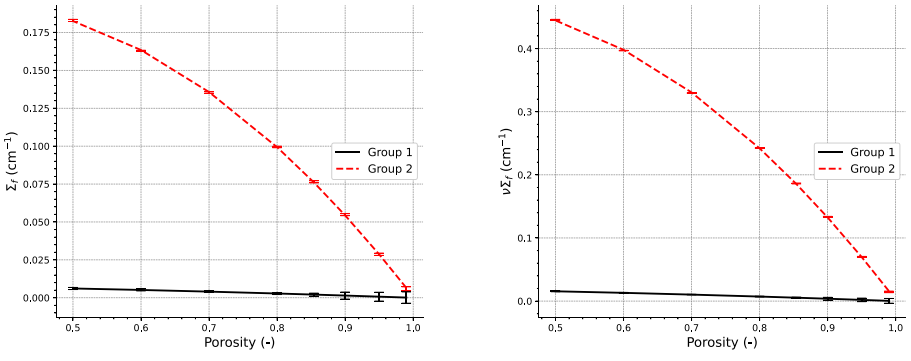

(c) Σ_{f}. (d) $\bar{\nu}\Sigma_{\mathrm{f}}$.

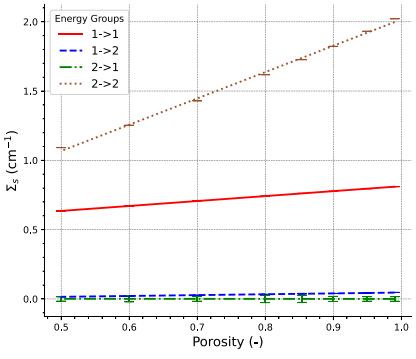

(e) $\Sigma_{\mathrm{s,g}\rightarrow\mathrm{g'}}$

Fig. 5. The fast and thermal macroscopic nuclear cross-sections of a powder particle surrounded by varying volumes of water, in an infinite medium. The points represent data calculated using Monte Carlo neutron transport code Serpent, the lines represent the correlations used in the proposed model.

Table 3
Macroscopic neutron cross-section correlation coefficients.

Cross-section (cm^{-1})	C_0	C_1	C_2
$\bar{\nu}\Sigma_{f,1}$	0.02297751	−0.00687425	−0.01613239
$\bar{\nu}\Sigma_{f,2}$	0.36194184	0.69095255	−1.05102329
$\Sigma_{a,1}$	0.01139081	0.0368169	−0.04634184
$\Sigma_{a,2}$	0.19590138	0.34348078	−0.51942155
$\Sigma_{f,1}$	0.00915864	−0.00287971	−0.00629015
$\Sigma_{f,2}$	0.14853871	0.2835586	−0.43132937
$\Sigma_{tr,1}$	0.35606652	−0.14885192	0.00405083
$\Sigma_{tr,2}$	0.76885785	−0.12069424	0.52981942
$\Sigma_{s,1\rightarrow1}$	0.45658621	0.35695688	0.0
$\Sigma_{s,1\rightarrow2}$	−0.01566651	0.06185078	0.0
$\Sigma_{s,2\rightarrow1}$	0.00191271	−0.00186743	0.0
$\Sigma_{s,2\rightarrow2}$	0.11795809	1.89864242	0.0

The appropriateness of the proposed macroscopic nuclear cross-section correlations was examined by comparing normalised scalar neutron flux distributions calculated using both Serpent and a deterministic steady-state, two-energy group, spatially-dependent, neutron diffusion code. Geometries with high levels of spatially varying powder particle number densities were specified, these can be seen in Fig. 6. Fig. 6 shows good agreement between the normalised scalar neutron flux profile calculated using the point-wise continuous energy Monte Carlo neutron transport code, Serpent, and the steady-state, two-group, spatially dependent, neutron diffusion code developed for the proposed model. This supports the use of these macroscopic nuclear cross-section correlations to calculate the normalised scalar neutron flux distribution, ultimately using the results to determine how the fission energy is distributed through the powder bed. The steady-state, spatially dependent, multi-group neutron diffusion equation is solved for every 0.5 $ change in the reactivity of the system.

4.4. Slumping and wetting-induced reactivity component

Volumetric slumping of the wetted powder results in varying fissile powder particle and water bulk densities in the wetted powder region. The effect that this reduction in porosity has on the reactivity of the system has been investigated here through a series of Monte Carlo neutron transport simulations using MCNP (Werner et al., 2018). The solid volume fraction of the slumped wetted UO_2 powder bed can be found for a given fractional slumping rate, f_{slump}, by re-writing Eq. (47) as:

$$\upsilon_{f,p,wp} = \frac{1}{1 - f_{slump}} \upsilon_{f,p,dp} \tag{76}$$

Therefore, by varying the bed immersion fraction for each prescribed slumped UO_2 powder bed solid volume fraction, it is possible to gain an understanding of the effect that powder bed collapse has on the reactivity throughout the wetting of the powder bed. MCNP simulation data presented in Fig. 7 suggests that slumping introduces a negative reactivity into the system, which counters the positive reactivity effect of water infiltration. This is shown by the fact that the immersion reactivity component is less for all cases where $f_{slump} > 0.0$ than for the case where $f_{slump} = 0.0$. The result is a greater level of powder bed saturation being required before criticality is reached. When the slumping fraction, $f_{slump} = 0.65$, the MCNP simulation data shown in Fig. 7 indicates that a nuclear criticality excursion will not occur, regardless of the bed immersion fraction. This is a consequence of the decreased porosity of the wetted UO_2 powder bed, preventing enough water (acting as moderator) from entering the pores to cause a nuclear criticality excursion.

Since each simulation has a constant prescribed slumped UO_2 powder bed solid volume fraction, it is possible to define a unique wetting-induced reactivity component for each powder bed undergoing different levels of volumetric collapse. The wetting-induced reactivity component may take the form outlined by (Jones et al., 2022):

Table 4
Coefficients for slumping-adjusted sub-critical wetting-induced reactivity contribution correlation (rounded to 5 s.f.).

i	Prescribed slumping fraction, f_{slump} (−)				
	0.0	0.2	0.4	0.5	0.6
0	−471.62	−470.95	−474.21	−472.23	−469.54
1	7520.8	6204.4	4902.2	2627.6	1687.5
2	−5.72e+04	−3.86e+04	−2.4169e+04	3.6926e+04	5.2608e+04
3	2.5869e+05	1.3986e+05	6.8483e+04	−7.6285e+05	−1.0385e+06
4	−7.3841e+05	−3.1042e+05	−1.1515e+05	6.6484e+06	1.0115e+07
5	1.3636e+06	4.2712e+05	1.1327e+05	−3.5854e+07	−6.351e+07
6	−1.625e+06	−3.5498e+05	−6.0129e+04	1.3203e+08	2.7766e+08
7	1.206e+06	1.631e+05	1.3294e+04	−3.4598e+08	−8.7571e+08
8	−5.0692e+05	−3.1794e+04	0.0	6.5686e+08	2.0292e+09
9	9.2149e+04	0.0	0.0	−9.0625e+08	−3.4805e+09
10	0.0	0.0	0.0	8.9918e+08	4.4091e+09
11	0.0	0.0	0.0	−6.246e+08	−4.0719e+09
12	0.0	0.0	0.0	2.8797e+08	2.6654e+09
13	0.0	0.0	0.0	−7.9063e+07	−1.1719e+09
14	0.0	0.0	0.0	9.7696e+06	3.1048e+08
15	0.0	0.0	0.0	0.0	−3.7472e+07
R^2	0.9999	0.9999	0.9999	0.9999	0.9999

$$R_{imm}(f_{imm}) = \sum_{i=0}^{n} C_i f_{imm}^i(t) \tag{77}$$

where $f_{imm}(t) = 1 - H_{dp}(t)/H_{dp+wp,0}$ is the bed immersion fraction, $H_{dp+wp,0}$ is the original height of the combined dry and wet powder, before any volumetric collapse of the powder bed has occurred.

Fig. 7 indicates that the reactivity of the UO_2 powder bed increases by around 500 $ as the immersion fraction ranges from 0.0 to 1.0. The reactivity feedback correlation coefficients used to model this reactivity component are outlined in Table 4. These correlation coefficients correspond to the line of best fit presented in Fig. 7. Good agreement is predicted when using these correlation coefficients, which is supported by the R^2 values tabulated in Table 4.

4.5. Other reactivity feedback effects

Voids generated through radiolysis and boiling provide pathways for neutrons to travel with a very low probability of collision, increasing neutron leakage. Jones et al. (2022) showed that the system reactivity is more sensitive to voids present within the interstices between pores than voids in the pooled water. Eq. (78) shows the general form of the reactivity feedback due to voids present in the wet powder and pooled water regions. Eqs. (79) and (80) describe the reactivity of the system as a function of bed immersion fraction and voids present in the pore and pooled water respectively. Table 5 outlines the coefficients used in Eqs. (79) and (80), that were originally determined by Jones et al. (2022) for the unslumped case.

$$\Delta R_{void,\ i}(\upsilon_{f,g}, f_{imm}) = R_{void,\ i}(\upsilon_{f,g}, f_{imm}) - R_{void,\ i}(\upsilon_{f,g,0}, f_{imm}) \tag{78}$$

where $\upsilon_{f,g,0}$ is the reference or initial voidage in the region being considered and subscript, i, may refer to the wet powder or pooled water regions.

$$\begin{aligned} R_{void,wp}(\upsilon_{f,g,wp}, f_{imm}) &= C_0 + C_1 f_{imm}(t) + C_2 \upsilon_{f,g,wp}(t) + C_3 f_{imm}^2(t) \\ &+ C_4 \upsilon_{f,g,wp}(t) f_{imm}(t) \\ &+ C_5 \upsilon_{f,g,wp}^2(t) + C_6 f_{imm}^3(t) + C_7 f_{imm}^2(t) \upsilon_{f,g,wp}(t) \\ &+ C_8 f_{imm}(t) \upsilon_{f,g,wp}^2(t) \end{aligned} \tag{79}$$

$$R_{void,sus}(\upsilon_{f,g,sus}, f_{imm}) = \left(C_0 f_{imm}^2(t) + C_1 f_{imm}(t) + C_2\right) \upsilon_{f,g,sus}(t) \tag{80}$$

The reactivity of the wetted powder bed also changes as a result of variations in phase temperatures within the system. The increasing phase temperatures lead to thermal expansion of the powder and water, as well as Doppler broadening of the nuclear cross-section resonances.

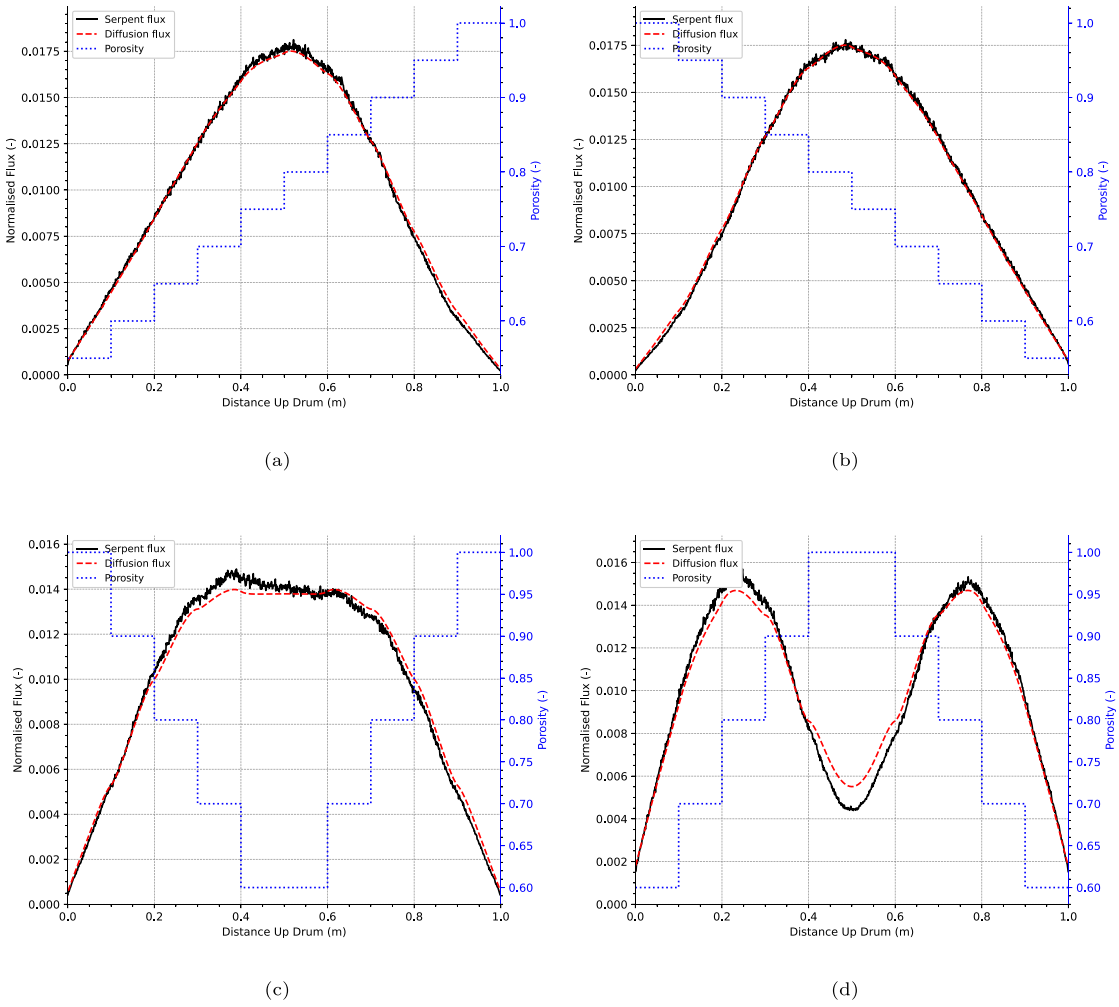

Fig. 6. Scalar Neutron flux distributions obtained through Monte Carlo neutron transport code Serpent alongside the multi-group neutron diffusion code using prescribed macroscopic nuclear cross-section correlations. The variation in the amount of UO_2 powder dispersed in the water is shown by the porosity.

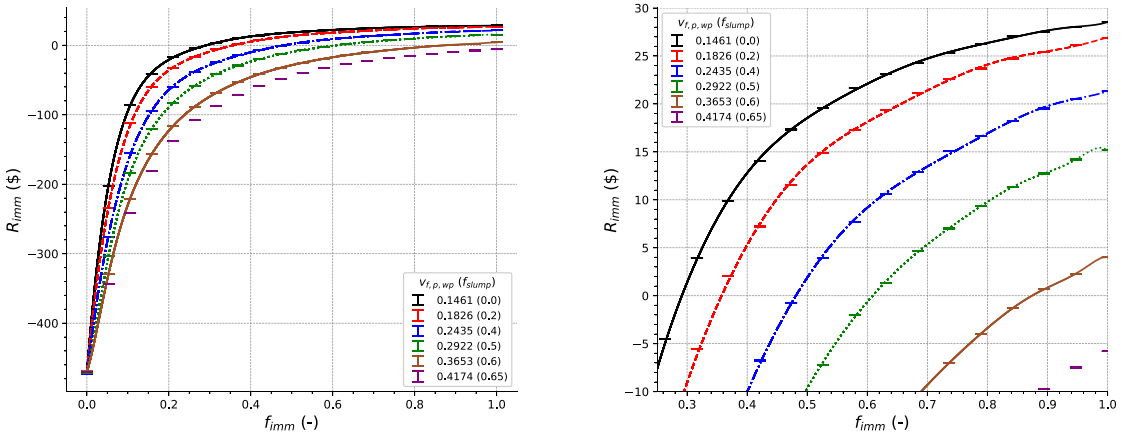

(a) Sub-critical reactivities. (b) Near- and post-critical reactivities.

Fig. 7. The sub-critical and post-critical wetting-induced reactivity component is shown for UO_2 powder beds with different volumetric slumping rates.

Table 5
Void feedback coefficients for voids present within pores and pooled water for water infiltration study.

Region	i	0	1	2	3	4	5	6	7	8
Wet powder	C_i	−72.72	362.1	−62.1	−464.4	224.1	−232.0	203.7	−155.4	108.7
Pooled water	C_i	−4.929841	12.476281	−7.983281	–	–	–	–	–	–

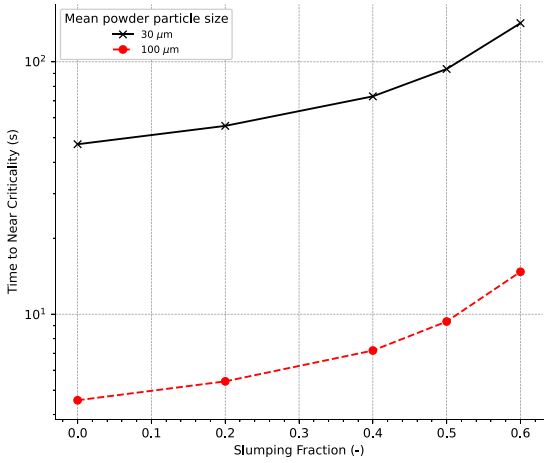

Fig. 8. The time taken for wetting and slumping to cause the initially unsaturated bed to reach a point near delayed critical.

Table 6
Thermal feedback coefficients for water infiltration study.

	C_0 ($\times 10^{-2}$)	C_1 ($\times 10^{-2}$)	C_2 ($\times 10^{-2}$)
Dry powder	0.4700	−0.8590	0.4219
Wet powder	0.1086	−0.5759	0.0
Pore water	−2.9357	4.8433	−2.5051

For UO_2 powder systems moderated by water, this tends to decrease the system reactivity. Jones et al. (2022) showed that with the exception of the dry powder region, increasing temperatures leads to a decreased powder bed reactivity. Thermal expansion in the dry powder region pushed powder particles into the wetted region, causing a positive reactivity effect. The general form of the thermal reactivity feedback is:

$$\Delta R_{\text{th, i}}(T_{\text{i}}, f_{\text{imm}}) = R_{\text{th, i}}(T_{\text{i}}, f_{\text{imm}}) - R_{\text{th, i}}(T_0, f_{\text{imm}}) \tag{81}$$

where T_0 is the reference temperature at the start of the simulation and the subscript i may refer to wet powder, dry powder or pore water. Eq. (82) from Jones et al. (2022) describes the specific correlation used to model the thermal reactivity feedback.

$$R_{\text{th, x}}(T_{\text{x}}, f_{\text{imm}}) = \left(C_2 f_{\text{imm}}^2(t) + C_1 f_{\text{imm}}(t) + C_0\right) T_{\text{i}}(t) \tag{82}$$

The corresponding coefficients for each region and phase, described in Jones et al. (2022), are summarised in Table 6.

4.6. Prescribed initial conditions

In a sub-critical fissile powder bed where no gas is being produced, and no significant thermal energy is generated, the model may be reduced to five spatially independent ordinary differential equations (ODEs). Represented by Eqs. (1), (2) and (43) to (45), these equations may be solved up to a point near delayed critical, where simulation using the full set of equations, including spatially-dependent nuclear thermal hydraulics, radiolytic gas and steam models will begin. These approach-to-critical simulations are performed to reduce the computational demands of the simulations by calculating initial conditions from where the full set of ODEs will be solved.

Initial region heights for the preliminary approach-to-critical simulation are those that represent a dry UO_2 powder bed where $H_{\text{dp}} = 0.6216$ m, $H_{\text{wp}} = 0.0001$ m (must be non-zero for Eq. (11) as noted by Jones et al. (2022)) and $H_{\text{sus}} = 0.3783$ m. The initial neutron density and delayed neutron precursor concentrations for the approach-to-critical simulation may be found using the following expressions:

$$n(0) = -\frac{s_{\text{n}}\Lambda}{R_{\text{T}}(0)\beta_{\text{eff}}} \tag{83}$$

and

$$C_{\text{i}}(0) = -\frac{\beta_{\text{i}} s_{\text{n}}}{\lambda_{\text{i}} R_{\text{T}}(0)\beta_{\text{eff}}} \tag{84}$$

where the value for the intrinsic neutron source density, $s_{\text{n}} = 0.135$ neutrons s^{-1} (cm^{-3} · UO_2). The initial reactivity at $t = 0$ s, for the approach-to-critical simulation, physically corresponding to a dry powder bed with a top reflector, is $R_{\text{T}} = -476$ \$. This value has been obtained by modelling the dry UO_2 powder bed using MCNP. The adjoint-weighted mean generation time and delayed neutron data are outlined in Tables 1 and 2. Using Eq. (83), this yields an initial neutron density, $n(0) = 2.06 \times 10^{-6}$ neutrons (cm^{-3} · UO_2) and corresponding group-wise delayed neutron precursor concentrations of $C_1(0) = 7.3 \times 10^{-4}$, $C_2(0) = 1.5 \times 10^{-3}$, $C_3(0) = 3.9 \times 10^{-4}$, $C_4(0) = 3.5 \times 10^{-4}$, $C_5(0) = 5.7 \times 10^{-5}$ and $C_6(0) = 7.1 \times 10^{-6}$ all with units precursor number per cubic centimetre of UO_2.

The approach-to-critical preliminary simulations were stopped once the reactivity became positive. The last negative reactivity evaluated by the ODE solver was used as the final data point of the sub-critical simulation. This value changed between each approach-to-critical simulation (see Tables 7 and 8) because of the temporal resolution of the ODE solver but remained close to zero for all cases modelled.

Initial conditions for the case where the mean powder diameter, $d_{\text{p}} = 100$ μm are presented in Table 8. Both powder beds modelled exhibit the same slumped wetted bed porosities. The dry and wetted powder bed region heights, shown in Tables 7 and 8 are very similar when close to criticality, irrespective of mean powder particle size.

The time to criticality (t_{crit}) as a function of the slumping fraction, shown in Fig. 8, suggests that wetting-induced slumping delays the start of the nuclear criticality excursion. The bed immersion fraction, $f_{\text{imm,0}}$,

Table 7
Initial system geometry and neutron kinetic data at a point close to criticality for variable slumping fractions with mean powder size, $d_{\text{p}} = 30$ μm.

$d_{\text{p}} = 30$ μm	Prescribed slumping fraction, f_{slump} (−)				
Property	0.0	0.2	0.4	0.5	0.6
C_1 (precursors cm^{-3} · UO_2)	0.02525	0.02879	0.03570	0.04864	0.08121
C_2 (precursors cm^{-3} · UO_2)	0.11383	0.12801	0.15529	0.20685	0.33089
C_3 (precursors cm^{-3} · UO_2)	0.07383	0.08073	0.09436	0.12030	0.17931
C_4 (precursors cm^{-3} · UO_2)	0.11090	0.11933	0.13626	0.16743	0.23518
C_5 (precursors cm^{-3} · UO_2)	0.02665	0.02822	0.03135	0.03689	0.04836
C_6 (precursors cm^{-3} · UO_2)	0.00448	0.00466	0.00504	0.00570	0.00703
$f_{imm,0}$ (−)	0.29127	0.30806	0.35748	0.43770	0.73535
H_{dp} (m)	0.44062	0.39943	0.32261	0.24319	0.07826
H_{wp} (m)	0.18108	0.17783	0.17949	0.18930	0.21744
H_{sus} (m)	0.27055	0.28835	0.31507	0.33743	0.38179
n (neutrons cm^{-3} · UO_2)	0.00158	0.00162	0.00170	0.00186	0.00219
R_{imm} (\$)	−0.00001	−0.00052	−0.00009	−0.00029	−0.00014
t_{crit} (s)	47.15337	55.74393	72.99537	93.68059	142.34885
$v_{f,p,wp}$ (−)	0.146	0.183	0.244	0.292	0.365

Table 8
Initial system geometry and neutron kinetic data at a point close to criticality for variable slumping fractions with mean powder size, $d_p = 100$ μm.

$d_p = 100$ μm	Prescribed slumping fraction, f_{slump} (−)				
Property	0.0	0.2	0.4	0.5	0.6
C_1 (precursors cm^{-3} · UO_2)	0.00299	0.00338	0.00419	0.00567	0.00978
C_2 (precursors cm^{-3} · UO_2)	0.01303	0.01501	0.01901	0.02627	0.04615
C_3 (precursors cm^{-3} · UO_2)	0.01057	0.01217	0.01535	0.02104	0.03558
C_4 (precursors cm^{-3} · UO_2)	0.02094	0.02375	0.02916	0.03878	0.06157
C_5 (precursors cm^{-3} · UO_2)	0.00703	0.00776	0.00916	0.01163	0.01704
C_6 (precursors cm^{-3} · UO_2)	0.00170	0.00183	0.00207	0.00247	0.00328
$f_{imm,0}$ (−)	0.29126	0.30806	0.35748	0.43770	0.73535
H_{dp} (m)	0.44062	0.39943	0.32261	0.24320	0.07826
H_{wp} (m)	0.18108	0.17783	0.17949	0.18930	0.21744
H_{sus} (m)	0.22818	0.23829	0.24960	0.25355	0.25484
n (neutrons cm^{-3} · UO_2)	0.00108	0.00110	0.00114	0.00120	0.00133
R_{imm} ($)	−0.00096	−0.00122	−0.00059	−0.00078	−0.00024
t_{crit} (s)	4.55825	5.41630	7.17682	9.35155	14.72212
$v_{f,p,wp}$ (−)	0.146	0.183	0.244	0.292	0.365

Table 9
Initial conditions for sub-critical partially wetted UO_2 powder bed.

Description	Symbol	Value
Initial dry powder region saturation	$S_{w,0}$	0
Reference temperature	T_0	293.15 K
All-region initial water temperature	T_w	293.15 K
All-region initial powder temperature	T_p	293.15 K
All region initial void-fraction	$v_{f,g}$	0

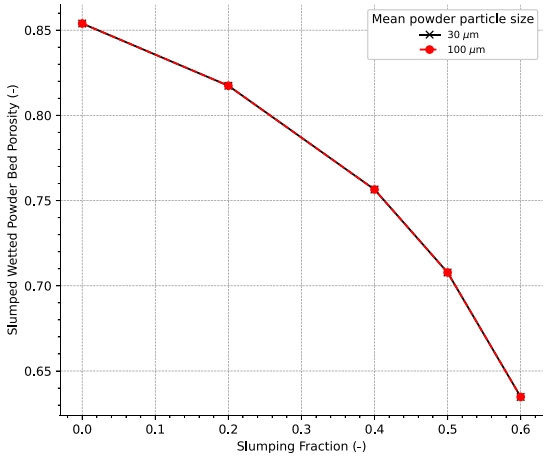

Fig. 9. The slumped wetted powder bed porosity as a function of the prescribed slumping fraction.

shown in Tables 7 and 8 is also higher at the point near criticality, as the slumping fraction increases.

Other initial conditions prescribed for the full simulation are summarised in Table 9. The initial saturation of the dry powder due to hygroscopic effects, $S_{w,0} = 0$. The reference temperature, T_0, refers to the initial homogeneous temperature of the system. The corresponding temperature of the water and powder throughout the system at the start of the simulation are denoted by T_w and T_p, respectively. Furthermore, since there are no voids present in the system initially, $v_{f,g} = 0$ throughout the domain.

5. Results

5.1. Wetting-induced volumetric slumping of powder beds

The initial conditions outlined for the powder beds in Section 4.6 yield the slumped wetted region porosities presented in Fig. 9. Fig. 9 confirms that the model implemented in this work produces a wetting-induced volumetric slump of the powder bed that is independent of the mean powder particle size. Furthermore, there is a non-linear relationship between the prescribed slumping fraction and the homogeneous wetted powder region porosity.

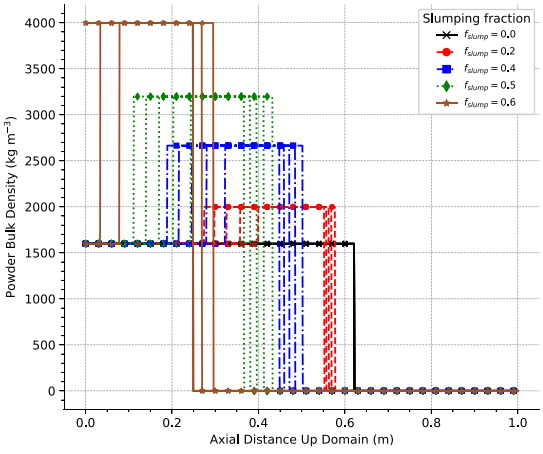

(a) $d_p = 30$ μm.

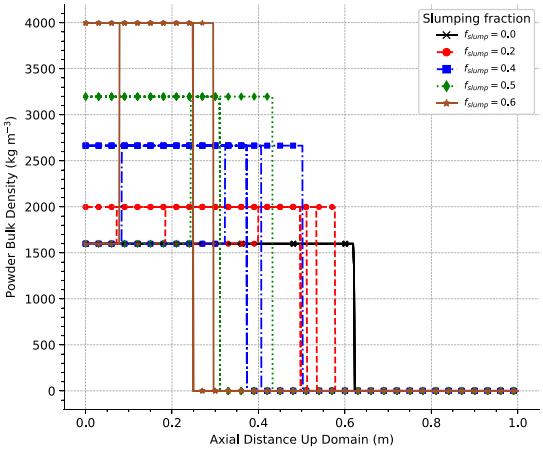

(b) $d_p = 100$ μm.

Fig. 10. The spatial variation in the UO_2 powder bulk density as a function of the prescribed slumping fraction. Multiple lines per slumping fraction correspond to the variation in powder bed bulk density over time, starting from $t - t_{crit} = 0$ s on the right of the graph, moving leftwards in increments of 25 s up to $t - t_{crit} = 100$ s.

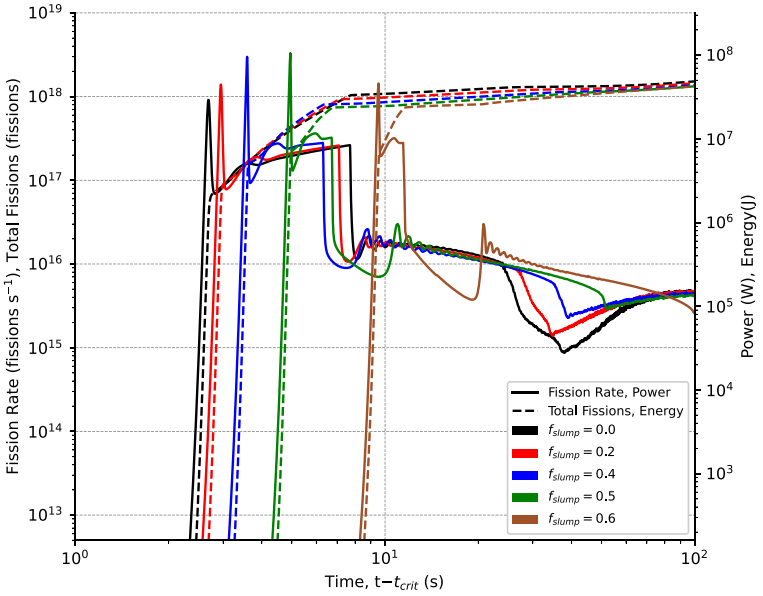

(a) Fission rate, integrated fissions, power and Energy.

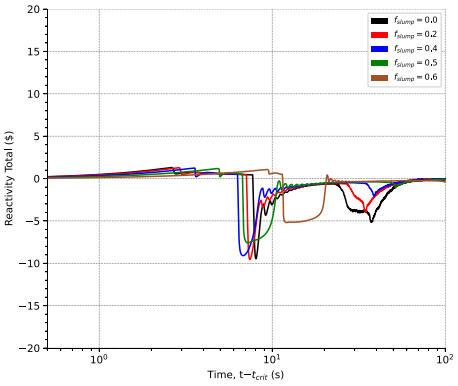

(b) Reactivity total.

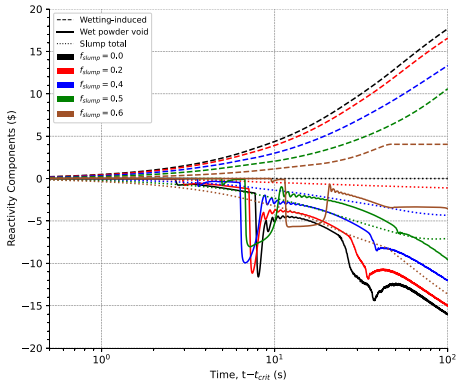

(c) Reactivity components.

Fig. 11. The fission power, energy and reactivity components 100 s post initial criticality for cases with varying slumping fraction, f_{slump}. All results are for the case where $d_{\text{p}} = 30$ μm.

Fig. 10 shows how the bulk density of the powder varies as a function of time throughout the domain, for each prescribed slumping fraction. The horizontal axes shown in Fig. 10 represent the position from the base of the domain at 0 m, where the dry powder sits, up to the top of the domain at 1 m, above the pooled water region. Repeated plots of the data moving to the left in Fig. 10 correspond to an increasing simulation time by increments of 25 s, starting from $t - t_{\text{crit}} = 0$ s and proceeding until $t - t_{\text{crit}} = 100$ s.

The powder bulk density, $\rho_{\text{p,bulk}} = 0$ kg m^{-3} in the pooled water region, which can be seen in either image in Fig. 10, at the upper portion of the domain. The set of vertical lines shown for each slumping fraction, located furthest right in the image, corresponds to the interface between the wetted powder and pooled water regions. Over time, for cases where $f_{\text{slump}} > 0$ this moves progressively downwards as the wetting-induced slump causes the powder bed to collapse. The solid black vertical line (the case where $f_{\text{slump}} = 0$) at 0.6217 m, reaching 1600 kg m^{-3}, remains the same irrespective of time, since no collapse takes place.

Furthermore, for cases where $f_{\text{slump}} > 0$, a set of secondary vertical lines appear in both images shown in Fig. 10, located lower down the domain. The vertical lines move further down the domain (to the left of the image) as time increases. This second vertical line corresponds to the location of the wetting front since the volumetric collapse (slump) occurs across the wetting front. The spatial bulk densities that are greater than the nominal dry powder bulk density of 1600 kg m^{-3} correspond to the slumped UO_2 powder bulk density for the prescribed slumping fraction. The location of the wetting front for the case where $f_{\text{slump}} = 0$ cannot be seen in Fig. 10, since there is no slumping to produce a second vertical line at the wetting front.

The location of the wetting front and wet powder–pooled water interfaces, whose locations have been previously stated, varies as a function of the prescribed mean UO_2 powder particle size. This is due to differences in the advection rate of water through the powder beds as a result of different permeabilities. The slumped powder bed bulk density is shown to not vary as a function of the mean powder particle size, which corresponds with Fig. 9.

5.2. Transient nuclear criticality excursion behaviour in slumping UO_2 powder beds

5.2.1. 30 μm Powder bed

Each simulation began from the calculated initial condition for the prescribed value of f_{slump} and was executed for $t - t_{\text{crit}} = 100$ s. The domain was split into 2000 axial slices (mesh cells). Increasing the spatial resolution further did not lead to different results whilst

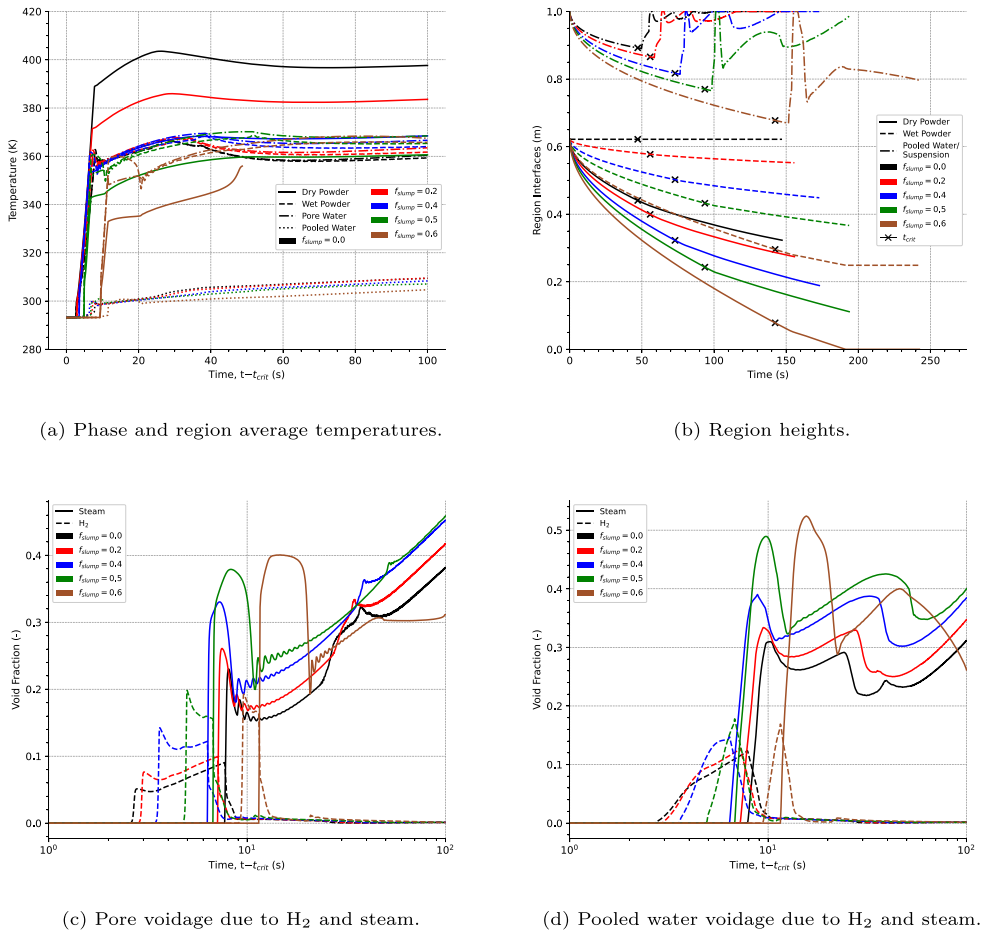

(a) Phase and region average temperatures.

(b) Region heights.

(c) Pore voidage due to H_2 and steam.

(d) Pooled water voidage due to H_2 and steam.

Fig. 12. Associated thermophysical system properties (for d_p = 30 μm powder bed) 100 s post initial criticality for cases with varying slumping fraction, f_{slump}.

significantly increasing the runtime of the simulations. Executing the simulation with a less refined spatial mesh led to deviations

Fig. 11(a) shows that there are similar characteristics between the nuclear criticality transient regardless of the amount of wetting-induced slumping. Fig. 11(a) also shows that the magnitude of the initial peak power varies as a function of the prescribed slumping fraction. The wetting-induced collapse of the powder bed led to an increase in the peak power, from 29.2 MW when f_{slump} = 0.0, to 106 MW when f_{slump} = 0.5. The fission energy deposited 100 s after the initial nuclear criticality excursion ranged from 48 MJ when f_{slump} = 0.0, to 42 MJ when f_{slump} = 0.6.

Volumetric collapse of the UO_2 powder bed significantly affects the reactivity of the system. This is evidenced in Fig. 11(c) by examining the slumping reactivity component, which is derived by subtracting the wetting-induced reactivity component (which accounts for slumping) for the case where f_{slump} = 0.0, with the wetting-induced reactivity for cases where $f_{slump} \neq 0.0$. The total reactivity of the system is the sum of the individual components in Fig. 11(c) (excluding the slumping component since this is accounted for in the wetting-induced reactivity component), and is shown in Fig. 11(b).

Fig. 11(a) shows that the peak power is reached shortly after the initiation of the nuclear criticality excursion. The dissociation of water molecules via radiolysis introduces voids into the system, adding negative reactivity which limits this power peak. This effect is shown by the increase in the H_2 void fraction in Fig. 12(c) and also Fig. 12(d) at a time that corresponds to the initial power peak. The negative void reactivity component is balanced by the increase in reactivity due to wetting, leading to a gradual increase in power until the onset of boiling. The initiation of boiling causes large voids to be created in the pores around powder particles (see Fig. 12(c)), introducing a correspondingly large negative reactivity into the system (see Fig. 11(c)), resulting in a reduction in power by greater than an order of magnitude. The reactivity feedback due to thermal effects and voids in the pooled water region are not shown in Fig. 11(c) since they are not significant in comparison to the effects of voids in the wet powder region and the combined effects of infiltration.

Average phase and region temperatures presented in Fig. 12(a) highlight the large amounts of thermal energy deposited into the dispersed multiphase media once the power peaks.

The height of each region and the time to criticality, t_{crit}, depicted in Fig. 12(b) suggests that for the case where f_{slump} = 0.6, the dry UO_2 powder bed will reach almost full saturation ($f_{imm,0}$ = 0.878) before a critical state is reached. The remaining wetting-induced reactivity that may be added to the system, once criticality is reached, in the case where f_{slump} = 0.6, is shown in Fig. 11(c) to be less than 5 $.

Simulated wetting-induced reactivity profiles for the other prescribed slumping fractions, shown in Fig. 11(c), suggest that a greater wetting-induced reactivity will be added to the system over the 100 s of simulated time. Furthermore, the wetting-induced reactivity addition rate, shown by the slopes of the dashed lines in Fig. 11(c), is higher as the prescribed slumping fraction tends to zero. These two factors imply that powder beds exhibiting less collapse will have higher reactivities at a given time after the initiation of the transient nuclear criticality excursion. Fig. 11(a) shows that the consequence of this is that higher fission energies are deposited in the systems with a lower prescribed slumping fraction. Figs. 12(a) and 12(c) shows that the pore voidage and dry UO_2 powder region temperatures are higher for the cases with a higher fission energy deposition. The wet UO_2 powder temperature,

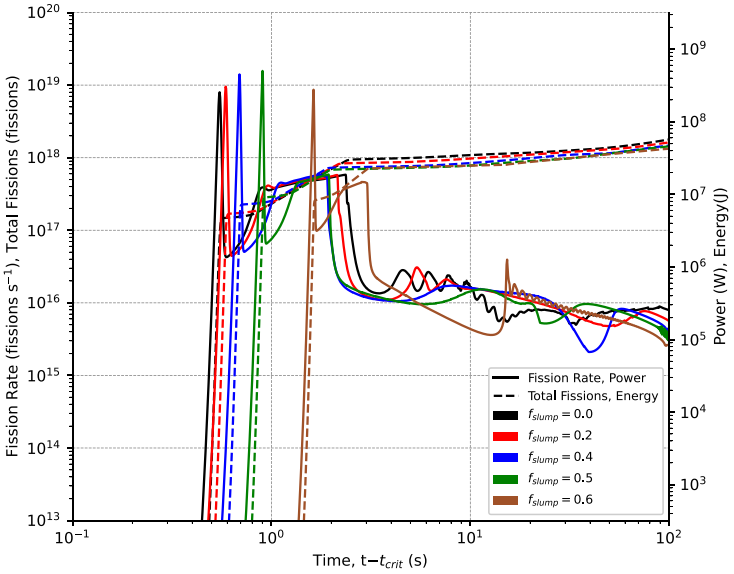

(a) Fission rate, integrated fissions, power and Energy.

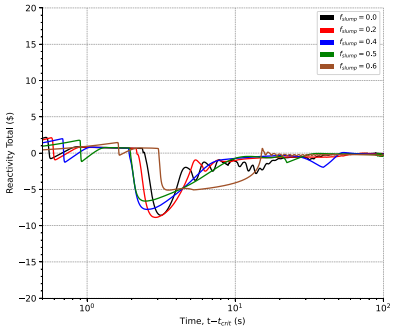

(b) Reactivity total.

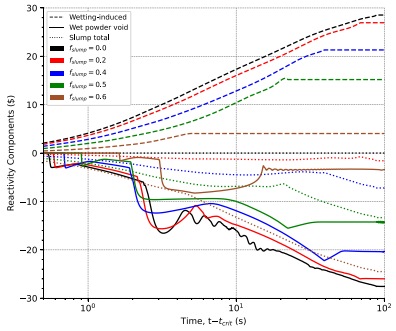

(c) Reactivity components.

Fig. 13. The fission power, energy and reactivity components 100 s post initial criticality for cases with varying slumping fraction, f_{slump}. All results are for the case where d_{p} = 100 μm.

shown in Fig. 12(a), is limited to the boiling point of water as a result of efficient interfacial convection between the phases.

5.2.2. 100 μm *Powder bed*

Data regarding the transient nuclear criticality excursion for the case where d_{p} = 100 μm is presented in Figs. 13 and 14. In this case, the nuclear criticality transient is initiated quicker than for the smaller sized UO_2 powder bed due to the increased rate of infiltration. This is a consequence of the comparatively higher rates of water infiltration, illustrated through a lower dry UO_2 powder region interface location at a given time in Fig. 14(b) when compared to Fig. 12(b).

Fig. 13(a) shows that there are similar characteristics between the nuclear criticality transient regardless of the amount of wetting-induced slumping. Fig. 13(a) also shows that the magnitude of the initial peak power varies as a function of the prescribed slumping fraction. The wetting-induced collapse of the powder bed led to an increase in the peak power, from 255 MW when $f_{\text{slump}} = 0.0$, to 501 MW when $f_{\text{slump}} = 0.5$. The fission energy deposited 100 s after the initial nuclear criticality excursion ranged from 57 MJ when $f_{\text{slump}} = 0.0$, to 43 MJ $f_{\text{slump}} = 0.6$.

Fig. 13(b) shows that slumping introduces a negative reactivity into the system. The slumping reactivity component is derived from the wetting-induced reactivity component, which already accounts for the effects of slumping (see Section 4.4). An oscillatory power response is observed in Fig. 13(a) within the interval of $t - t_{\text{crit}} = 4$ s to $t - t_{\text{crit}} = 30$ s. This oscillatory response is attributed to oscillations in the creation of steam interstitially between UO_2 powder particles (see Fig. 14(c)), which introduces an oscillatory wetted powder region void reactivity feedback component, as shown in Fig. 13(b). The gas present in the wetted powder region advects into the pooled water region, shown in Fig. 14(d).

Full saturation of the UO_2 powder bed is shown in Fig. 14(b), for each prescribed slumping fraction, by the solid lines intersecting with the x-axis. At this point in time, the dashed lines, representing the height of the wetted UO_2 powder region, become constant in time. Physically this represents that the wetted powder bed has become static and the wetting-induced volumetric collapse has ceased.

The reactivity feedback due to thermal effects and voids in the pooled water region are not shown in Fig. 13(b) since they are not significant in comparison to the effects of voids in the wet powder region, infiltration and slumping.

5.2.3. *Peak power to boiling time*

Figs. 11(a) and 13(a) show that there is a period of time early during the transient nuclear criticality excursion, just after the first power peak, where the power of the system increases to around 10 MW, before there is a second sharp drop in power. Figs. 11(c) and 13(b) suggest that during this time, wetting-induced reactivity is matched by a negative reactivity due to voids present in the wet powder.

Competing reactivity components at this time cause the total reactivity of the system, shown in Figs. 11(b) and 13(c), to indicate that a delayed critical state is reached (0$ ≤ R_{T} < 1 $). The delayed critical state remains until the second sharp drop in power. The time at which

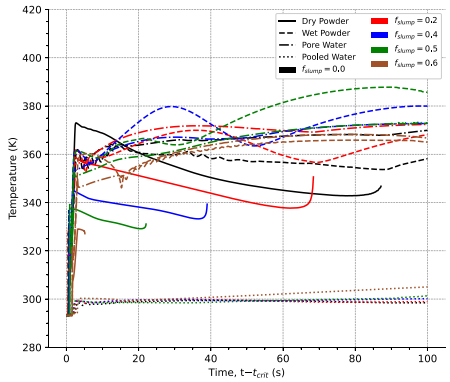

(a) Phase and region average temperatures.

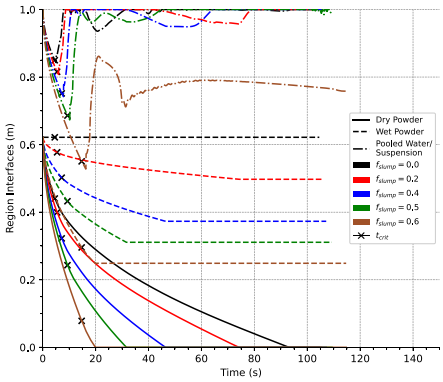

(b) Region heights.

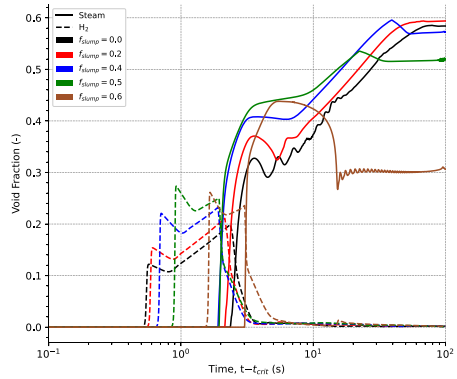

(c) Pore voidage due to H_2 and steam.

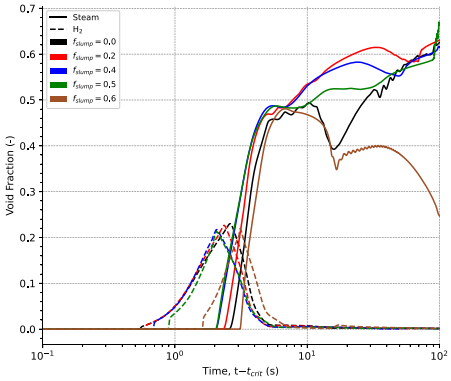

(d) Pooled water voidage due to H_2 and steam.

Fig. 14. Associated thermophysical system properties (for $d_p = 100$ μm powder bed) 100 s post initial criticality for cases with varying slumping fraction, f_{slump}.

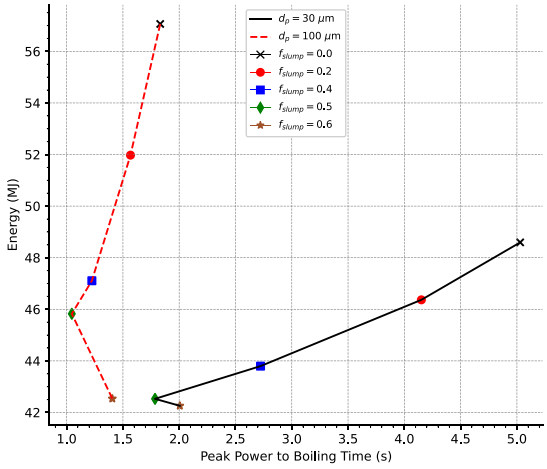

Fig. 15. The total fission energy generated is plotted as a function of the time taken for the onset of boiling, from the initial power peak.

this sharp drop in power occurs coincides with the creation of steam in the pores, shown in Figs. 12(c) and 14(c), indicating that boiling occurs at this time. The time taken for boiling to occur and for the second sharp drop in power to occur is for each simulated case is shown in Fig. 15.

Fig. 15 indicates the total energy deposited for the 100 s after the initial nuclear criticality excursion as a function of the time between peak power and boiling. Generally, as the time from the initial power peak to the onset of boiling decreases, less fission energy is generated. The case where $f_{\text{slump}} = 0.6$ is an exception where a greater peak power to boiling time results in less fission energy generated over the simulated time than for the case where $f_{\text{slump}} = 0.5$. This is due to the low rate of reactivity insertion predicted for the case where $f_{\text{slump}} = 0.6$ when the initial delayed critical point is reached. With a lower rate of reactivity insertion predicted, the amount of time required for boiling to be reached is greater.

Figs. 11(a) and 13(a) show that the fission energy deposited into the system over the 100 s of simulation time decreases as the prescribed slumping fraction increases. This may be attributed to the fact that the slumping reactivity component, shown in Figs. 11(c) and 13(b), is lower with increased slumping fraction.

5.3. Hydrostatic pressure in wetted powder bed

The gauge hydrostatic pressure of the powder bed is calculated from the surface of the pooled water to the interface between the wet and dry powder regions (the wetting front). Fig. 16 highlights how the hydrostatic pressure at the final time, $t-t_{\text{crit}} = 100$ s, varies as a function of the prescribed slumping fraction. The hydrostatic gauge pressure increases as the evaluation point moves further down the domain. The slope of the curve represents the rate of change in hydrostatic pressure axially down the domain. This is affected by the contents of the domain at the point of interest (see Eq. (65)). Eq. (65) also indicates that the hydrostatic pressure gradient in locations with increased gas content is less than in locations with greater water content. The lowest point plotted in Fig. 16 is the location of the wetting front and therefore represents the hydrostatic pressure at the wetting front. This point also corresponds to the maximum hydrostatic pressure.

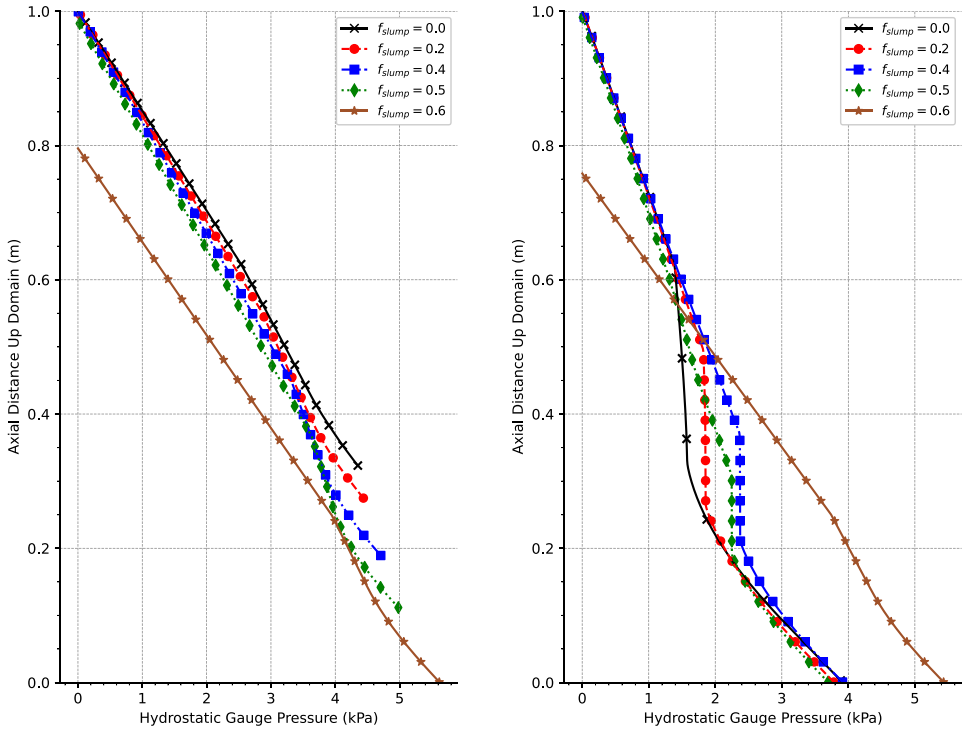

(a) $d_p = 30$ μm. (b) $d_p = 100$ μm.

Fig. 16. The hydrostatic gauge pressure is shown at the final time, $t - t_{crit} = 100$ s. The reference point is taken from the top of the pooled water region.

Fig. 16(a) shows that an increase in the slumping fraction produces a larger hydrostatic pressure at the wetting front for the case where $d_p = 30$ μm. This may be attributed to the fact that the wetting front has progressed further down the domain, producing a greater gravitational potential at the wetting front. The larger gravitational potential at the wetting front for increasing slumping fraction exists despite the increased voidage with an increased slumping fraction (for cases where $f_{slump} < 0.6$) shown in Figs. 12(c) and 12(d). This suggests that the increased percolation height is more dominant in determining the hydrostatic pressure at the wetting front than voids for these specific cases.

Fig. 16(b) suggests that the hydrostatic pressure at the wetting front does not significantly vary with varying slumping fraction when $f_{slump} < 0.6$. Differences that are present may be attributed to the voidage in the pores and pooled water regions, shown in Figs. 14(c) and 14(d), respectively. The hydrostatic pressure when $f_{slump} = 0.6$ is far greater than in the other cases because of the lower voidage present at $t - t_{crit} = 100$ s.

6. Conclusions

The characteristics of transient nuclear criticality excursions in wetted 5-wt% enriched UO_2 powder beds was shown to depend strongly on the amount of slumping that occurs as a result of wetting-induced volumetric collapse. Therefore, transient criticality safety studies modelling wetting-induced nuclear criticality excursions in UO_2 powders and potentially other fissile powders, should take the re-distribution of fissile material, due to slumping, into consideration.

Volumetric collapse of the UO_2 powder bed was shown to introduce a negative reactivity into the system. The results of MCNP simulations identified that large amounts of wetting-induced collapse could prevent the UO_2 powder bed from reaching a critical state, regardless of the powder bed saturation. Furthermore, the volumetric collapse of the wetted UO_2 powder bed delayed the initiation of the transient nuclear criticality excursions.

The model predicted that the peak power and fission energy were sensitive to the level of slumping and the mean size of UO_2 powder particles. For the case where $d_p = 30$ μm, the total energy released varied from 42 MJ to 48 MJ and initial peak powers varied widely from 29.2 MW to 106 MW, with the largest power predicted for the case where the slumping fraction, $f_{slump} = 0.5$. For the 100 μm UO_2 powder bed, the peak power increased from 255 MW for the unslumped case to 501 MW for the case where $f_{slump} = 0.5$. Integrated fission power, or energy released, over the period of 100 s after the initial nuclear criticality excursion, varied from 57 MJ to 42 MJ as the slumping fraction varied from $f_{slump} = 0.0$ to $f_{slump} = 0.6$, for the case where $d_p = 100$ μm.

Declaration of competing interest

The authors declare that they have no known competing financial interests or personal relationships that could have appeared to influence the work reported in this paper.

Data availability

In accordance with EPSRC funding requirements, all supporting data used to create figures in this paper may be accessed at the following URL: https://doi.org/10.5281/zenodo.7104999.

Acknowledgements

Mr G.S. Jones gratefully acknowledges the financial support of the Engineering and Physical Science Research Council (EPSRC) and AWE plc through the industrial CASE PhD programme (EPSRC Grant No.: EP/S513635/1).

References

Al-Rawas, A.A., 2000. State-of-the-art-review of collapsible soils. Sultan Qaboos Univ. J. Sci. (SQUJS) 5, 115–135.

ANS, 2018. Nuclear Criticality Safety in Operations with Fissionable Materials Outside Reactors ANSI/ANS-8.1. American Nuclear Society (ANS), 555 North Kensington Avenue, La Grange Park, Illinois, 60526, USA.

Barden, L., McGowan, A., Collins, K., 1973. The collapse mechanism in partly saturated soil. Eng. Geol. 7, 49–60.

Basoglu, B., 1992. Analysis of a Hypothetical Criticality Accident Involving Damp Low-enriched UO_2 Powder (Master's Thesis). University of Tennessee.

Basoglu, B., Brewer, R.W., Haught, C.F., Hollenbach, D.F., Wilkinson, A.D., Dodds, H.L., Pasqua, P.F., 1994. Simulation of hypothetical criticality accidents involving homogeneous damp low-enriched UO_2 powder systems. Nucl. Technol. 105 (1), 14–30.

Bell, G.I., Glasstone, S., 1970. Nuclear Reactor Theory, first ed. Van Nostrand Reinhold Company, Litton Educational Publishing Inc..

Bentridi, S.-E., Gauthier-Lafaye, F., Gall, B., Seghour, A., 2011. Monte-Carlo based numerical modeling and simulation of criticality conditions occurrence in natural reactor zone 9 in Oklo deposit (Gabon). Prog. Nucl. Sci. Technol. 2, 395–400. http://dx.doi.org/10.15669/PNST.2.395.

Bresson, L.M., Moran, C.J., 2004. Micromorphological study of slumping in a hardsetting seedbed under various wetting conditions. Geoderma 118, 277–288.

Brooks, R., Corey, T., 1964. Hydraulic Properties of Porous Media. In: Hydrology Papers 3, Colorado State University, Fort Collins.

Cho, S.E., Lee, S.R., 2001. Instability of unsaturated soil slopes due to infiltration. Comput. Geotech. 28, 185–208.

Coindreau, O., Fichot, F., Fleurot, J., 2013. Nuclear fuel rod fragmentation under accidental conditions. Nucl. Eng. Des. 255, 68–76.

Courant, R., Friedrichs, K., Lewy, H., 1928. Über die partiellen differenzengleichungen der mathematischen physik. Math. Ann. 100 (1), 32–74.

Datta, A., 1991. A review of fire hazards and fire protection concerns of commercial fuel cycle facilities in the United States. Nucl. Eng. Des. 125 (3), 315–323.

Doucet, M., Zheng, S., Mouton, J., Porte, R., 2003. Framatome-ANP France UO_2 fuel fabrication - criticality safety analysis in the light of the JCO accident. Japan Atomic Energy Research Agency (JAERI), Kashiwa, Chiba (Japan). In: International Conference on Nuclear Criticality Safety (ICNC2003). Challenges in the Pursuit of Global Nuclear Criticality Safety. Tokai, Ibaraki (Japan), pp. 755–757.

Duderstadt, J.J., Hamilton, L., 1976. Nuclear Reactor Analysis. John Wiley & Sons.

Duhamel, I., Rouyer, V., Santamarina, A., Venard, C., 2004. Criticality calculation codes validation: Experimental needs for low-moderated MOX media. In: Workshop on the Need of Integral Critical Experiments with Low-Moderated MOX Fuels. OECD/NEA, Issy-les-Moulineaux, France, pp. 55–66.

Dunn, E., Brown, S., Dodds, M., Thomas, A., 2013. Credible moderation content of uranium oxide powder and pellet systems. In: Topical Meeting held by the ANS Nuclear Criticality Safety Division (NCSD 2013), Criticality Safety in the Modern Era: Raising the Bar. American Nuclear Society, Wilmington, North Carolina, USA, pp. 380–393.

Ebisuzaki, T., Maruyama, S., 2017. Nuclear geyser model of the origin of life: Driving force to promote the synthesis of building blocks of life. Geosci. Front. 8 (2), 275–298, Frontiers in Early Earth History and Primordial Life - Part I.

Fink, J.K., Chasanov, M.G., Leibowitz, L., 1981. Thermophysical properties of uranium dioxide. J. Nuclear Mater. 102 (1), 17–25.

Fredlund, D.G., Morgenstern, N.R., 1976. Constitutive relations for volume change in unsaturated soils. Can. Geotech. J. 13 (3), 261–276.

Fredlund, D.G., Rahardjo, H., Fredlund, M.D., 2012. Unsaturated Soil Mechanics in Engineering Practice, first ed. John Wiley & Sons, Ltd.

Frid, W., Höjerup, F., Lindholm, I., Miettinen, J., Nilsson, L., Puska, E., Sjövall, H., 2001. Severe accident recriticality analyses (SARA). Nucl. Eng. Des. 209 (1), 97–106.

Fukuda, K., Nishiyama, J., Obara, T., 2021. Supercritical transient analysis for ramp reactivity insertion using multiregion integral kinetics code. Nucl. Sci. Eng. 195 (5), 453–463.

Gil, L., 2018. Meet Oklo, the Earth's two-billion-year-old only known natural nuclear reactor. IAEA Bull. 27.

Green, W.H., Ampt, G.A., 1911. Studies on soil physics. Part I. The flow of air and water through soils. J. Agricul. Sci. 4 (1), 1–24.

Handley, G.R., 1972. Some effects of water sprinklers on array criticality safety analyses. Nucl. Technol. 14 (1), 71–75.

Hirt, C., Nichols, B., 1981. Volume of fluid (VOF) method for the dynamics of free boundaries. J. Comput. Phys. 39 (1), 201–225.

Holmes, W.D., McLaughlin, T.P., 1994. Nuclear criticality safety guide for fire protection professionals in DoE nuclear facilities. U.S. Department of Energy.

Houston, W.N., Mahmoudand, H.H., Houston, S., 1993. Laboratory procedure for partial-wetting collapse determination. In: Proceedings of the 1993 ASCE National Convention and Exposition, Unsaturated Soils. pp. 54–63.

IAEA, 2008. Safety of nuclear fuel cycle facilities. In: Number SSR-4 in Specific Safety Requirements. International Atomic Energy Agency (IAEA), Vienna.

IAEA, 2010. Safety of uranium and plutonium mixed oxide fuel fabrication facilities. In: Number SSG-7 in Specific Safety Guides. International Atomic Energy Agency (IAEA), Vienna.

IAEA, 2014. Criticality Safety in the Handling of Fissile Material. In: Number SSG-27 in Specific Safety Guides, International Atomic Energy Agency (IAEA), Vienna.

Ibekwe, R.T., Cooling, C.M., Trainer, A.J., Eaton, M.D., 2020. Modeling the short-term and long-term behaviour of the Oklo natural nuclear reactor phenomenon. Prog. Nucl. Energy 118, 103080.

Ingram, D.M., Causon, D.M., Mingham, C.G., 2003. Developments in cartesian cut cell methods. Math. Comput. Simulation 61 (3), 561–572, Modelling 2001 - Second IMACS Conference on Mathematical Modelling and Computational Methods in Mechanics, Physics, Biomechanics and Geodynamics.

Jones, G.S., Winter, G.E., Cooling, C.M., Williams, M.M.R., Eaton, M.D., 2022. Mathematical and computational models for simulating transient nuclear criticality excursions within wetted fissile powder systems. Annals of Nuclear Energy 169, 108796.

Karema, H., Lo, S., 1999. Efficiency of interphase coupling algorithms in fluidized bed conditions. Comput. & Fluids 28 (3), 323–360.

Kiedrowski, B.C., Brown, F.B., Wilson, P.P.H., 2011. Adjoint-weighted tallies for k-eigenvalue calculations with continuous-energy Monte Carlo. Nucl. Sci. Eng. 168 (3), 226–241.

Kleinstreuer, C., 2003. Two-Phase Flow: Theory and Applications, first ed. Taylor & Francis.

Kuroda, P.K., 1956. On the nuclear physical stability of the uranium minerals. J. Chem. Phys. 25 (4), 781–782.

Lane, J.A., MacPherson, H.G., Maslan, F., 1958. Fluid Fuel Reactors, first ed. In: Addison-Wesley books in nuclear science and metallurgy, Addison-Wesley Pub. Co..

Lawton, E.C., Fragaszy, R.J., Hetherington, M.D., 1992. Review of wetting-induced collapse in compacted soil. J. Geotechn. Eng. 118 (9), 1376–1394.

Leppänen, J., Pusa, M., Viitanen, T., Valtavirta, V., Kaltiaisenaho, T., 2015. The serpent Monte Carlo code: Status, development and applications in 2013. Ann. Nucl. Energy 82, 142–150.

Li, P., Vanapalli, S., Li, T., 2016. Review of collapse triggering mechanism of collapsible soils due to wetting. J. Rock Mech. Geotechn. Eng. 8 (2), 256–274.

Marshall, A.C., 2008. Space Nuclear Safety, first ed. Krieger Publishing.

Marsily, G.D., 1986. Quantitative Hydrogeology, first ed. Academic Press.

Maruyama, S., Kurokawa, K., Ebisuzaki, T., Sawaki, Y., Suda, K., Santosh, M., 2019. Nine requirements for the origin of Earth's life: Not at the hydrothermal vent, but in a nuclear geyser system. Geosci. Front. 10 (4), 1337–1357.

Mason, R.M., Martin, J.K., Smith, P.N., Turland, B.D., 2012a. Comparison of a post-closure transient criticality model with the Oklo natural reactors. Mineral. Mag. 76 (8), 3145–3153.

Mason, R.M., Smith, P.N., 2015. Modelling of consequences of hypothetical criticality: post-closure criticality consequence analysis for ILW, LLW and DNLEU Disposal. AMEC Report Radioactive Waste Management Ltd, RWM005140.

Mason, R.M., Smith, P.N., Sweet, D.W., Eaton, M.D., Goddard, A.J.H., Gomes, J.L.M.A., Pain, C.C., 2009. A summary of verification, validation, benchmarking, uncertainty and sensitivity for the FETCH, QSS and RTM computer models. Serco Report for the Nuclear Decommissioning Authority (NDA), SERCO/TAS/P3648/W001 Issue 2.

Mason, R.M., Smith, P.N., Turland, B.D., Jackson, C.P., 2012b. The consequences of hypothetical post-closure criticality. Mineral. Mag. 76 (8), 3155–3163.

Naudet, R., 1991. Oklo: Des Réacteurs Nucléaires Fossiles. In: Collection du Commissariat à l'énergie atomique. Série Synthèses, Eyrolles.

Odong, J., 2007. Evaluation of empirical formulae for determination of hydraulic conductivity based on grain-size analysis. J. Am. Sci. 3 (3), 54–60.

Pereira, J.H.F., Fredlund, D.G., 2000. Volume change behaviour of collapsible compacted Gneiss soil. J. Geotech. Geoenviron. Eng. 126 (10), 907–916.

Raap, M.B., Heinrichs, D.P., McLaughlin, T.P., Morman, J.A., 2014. CSSG position on use of water for firefighting in light of criticality constraints for DoE facilities. U.S. Department of Energy, CSSG.

Rao, S.M., Revanasiddappa, K., 2000. Role of matric suction in collapse of compacted clay soil. J. Geotech. Geoenviron. Eng. 126 (1), 85–90.

Rozain, J., Fouillaud, P., Barbry, F., Mather, D., Bickley, A., Prescott, A., 1991. Criticality excursions in wetted UO_2 powder. Trans. Am. Nuclear Soc. 63, 228.

Sakai, M., Yamamoto, T., Murazaki, M., Miyoshi, Y., 2004. Effect of particulate behavior on criticality evaluation in agitating powder of nuclear fuel. Powder Technol. 148 (1), 67–71.

Schwinkendorf, K.N., 1999. Recriticality energetics of a hypothetical water reflood accident in a damaged light water reactor. Nucl. Sci. Eng. 132 (1), 118–126.

Shampine, L., Gordon, M., 1975. Computer Solution of Ordinary Differential Equations: The Initial Value Problem, first ed. W H Freeman and Co Ltd.

Stacey, W.M., 2018. Nuclear Reactor Physics, third ed. Wiley-VCH.

Sun, D.M., Li, X.M., Feng, P., Zang, Y.G., 2016. Stability analysis of unsaturated soil slope during rainfall infiltration using coupled liquid-gas-solid three-phase model. Water Sci. Eng. 9 (3), 183–194.

Tadepalli, R., Fredlund, D.G., 1991. The collapse behaviour of a compacted soil during inundation. Can. Geotech. J. 28 (4), 477–488.

Tadepalli, R., Rahardjo, H., Fredlund, D.G., 1992. Measurements of matric suction and volume changes during inundation of collapsible soil. Geotech. Test. J. 15 (2), 115–122.

Tuya, D., Obara, T., 2017. Supercritical transient analysis in coupled fuel debris systems of symmetric and asymmetric geometry using integral kinetic model. Ann. Nucl. Energy 109, 113–119.

Werner, C.J., Armstrong, J., Brown, F.B., Bull, J.S., Casswell, L., Cox, L.J., Dixon, D., Forster, R.A., Goorley, J.T., Hughes, H.G., Favorite, J., Martz, R., Mashnik, S.G., Rising, M.E., Solomon, C., Sood, A., Sweezy, J.E., Zukaitis, A., Anderson, C., Elson, J.S., Durkee, J.W., Johns, R.C., McKinney, G.W., McMath, G.E., Hendricks, J.S., Pelowitz, D.B., Prael, R.E., Booth, T.E., James, M.R., Fensin, M.L., Wilcox, T.A., Kiedrowski, B.C., 2018. MCNP6.2 Release Notes. Report LA-UR-18-20808, Los Alamos National Laboratory (LANL).

Yamane, Y., Yamamoto, T., Miyoshi, Y., 2003. Development of numerical simulation codes for estimation of number of fission released at criticality accident of MOX powder system. Japan Atomic Energy Research Institute (JAERI) Report.

Yeoh, G.H., Tu, J., 2019. Computational Techniques for Multiphase Flows, second ed. Butterworth-Heinemann.

Zeitoun, O., Shoukri, M., Chatoorgoon, V., 1994. Measurement of interfacial area concentration in subcooled liquid-vapour flow. Nucl. Eng. Des. 152 (1), 243–255.